HHS Public Access

Author manuscript

Sci Transl Med. Author manuscript; available in PMC 2022 March 13.

Published in final edited form as:

Sci Transl Med. 2021 October 13; 13(615): eabf7860. doi:10.1126/scitranslmed.abf7860.

Epigenetically defined therapeutic targeting in H3G34R/V high-grade gliomas

Stefan R. Sweha[1,2], **Chan Chung**[1,3], **Siva Kumar Natarajan**[1,4], **Pooja Panwalkar**[1], **Matthew Pun**[1,5,6], **Amer Ghali**[1], **Jill Bayliss**[1], **Drew Pratt**[1,7], **Anand Shankar**[8], **Visweswaran Ravikumar**[9], **Arvind Rao**[8,9,10], **Marcin Cieslik**[7,8], **Kari Wilder-Romans**[10], **Andrew J. Scott**[10], **Daniel R. Wahl**[10], **Selin Jessa**[11,12], **Claudia L. Kleinman**[12,13], **Nada Jabado**[13,14], **Alan Mackay**[15], **Chris Jones**[15], **Daniel Martinez**[16], **Mariarita Santi**[16], **Alexander R. Judkins**[17], **Viveka Nand Yadav**[18], **Tingting Qin**[8], **Timothy N. Phoenix**[19], **Carl J. Koschmann**[18], **Suzanne J. Baker**[20], **Arul M. Chinnaiyan**[7,21], **Sriram Venneti**[1,2,7,*]

[1]Laboratory of Brain Tumor Metabolism and Epigenetics, Department of Pathology, University of Michigan Medical School, Ann Arbor, MI 48109, USA.

[2]Neuroscience Graduate Program, University of Michigan, Ann Arbor, MI 48109, USA.

[3]Department of New Biology, Daegu Gyeongbuk Institute of Science and Technology (DGIST), Daegu 42988, Korea.

[4]Molecular and Cellular Pathology Graduate Program, University of Michigan Medical School, Ann Arbor, MI 48109, USA.

[5]Cellular and Molecular Biology Program, University of Michigan Medical School, Ann Arbor, MI 48109, USA.

[6]Medical Scientist Training Program, University of Michigan Medical School, Ann Arbor, MI 48109, USA.

[7]Department of Pathology, University of Michigan Medical School, Ann Arbor, MI 48109, USA.

[8]Department of Computational Medicine & Bioinformatics, University of Michigan Medical School, Ann Arbor, MI 48109, USA.

[9]Department of Biostatistics, University of Michigan, Ann Arbor, MI 48109, USA.

[*]Corresponding author: Sriram Venneti, M.D., Ph.D., svenneti@med.umich.edu.

Authors contributions: SRS and SV conceived the project, analyzed data, constructed figures, and wrote the manuscript; SRS, CC, PP, JB, AG, KWR, SKN, DM, VNY and AJS performed experiments and analyzed data; SRS, MP, DP, VR, AS, AR, MC, TQ, and CK performed bioinformatics; AM, SJB, VY, CJ and CJK provided cell lines or ChIP-seq data; CC, CJK, VY, DW, and SJB provided guidance on animal experiments; TNP provided plasmids for *IUE* models; MS and ARJ provided tumor samples for IHC; SJ, CLK and NJ provided human single cell data; GS, CC, DRW, AMC and AG provided valuable feedback on the manuscript. All authors read and approved the final manuscript.

List of Supplementary Materials
Materials and Methods
Fig. S1 to S6.
Table S1.
Data file S1.

Competing interests: DRW has received consulting fees from Agios Inc. He is an inventor on a patent (pending) related to methods of determining optimal treatment for brain tumor patients. AR serves as Member for Voxel Analytics, LLC and consulting relationship with Genophyll, LLC. The other authors declare no competing interests.

[10]Department of Radiation Oncology, University of Michigan Medical School, Ann Arbor, MI 48109, USA.

[11]Quantitative Life Sciences, McGill University, Montreal, Quebec H3A 0G4, Canada.

[12]Lady Davis Research Institute, Jewish General Hospital, Montreal, QC H3T 1E2, Canada.

[13]Department of Human Genetics, McGill University, Montreal, Quebec H3A 0G4, Canada.

[14]Department of Pediatrics, McGill University, and The Research Institute of the McGill University Health Centre, Montreal, Quebec H3A 0G4, Canada.

[15]Division of Molecular Pathology & Cancer Therapeutics, The Institute of Cancer Research, London, SM2 5NG, United Kingdom.

[16]Department of Pathology, Children's Hospital of Philadelphia, Philadelphia, PA 19104, USA.

[17]Department of Pathology, Children's Hospital of Los Angeles, Los Angeles, PA 90027, USA.

[18]Department of Pediatrics, University of Michigan Medical School, Ann Arbor, MI 48109, USA.

[19]Division of Pharmaceutical Sciences, College of Pharmacy, Cincinnati Children's Hospital Medical Center, Cincinnati, OH 45229, USA.

[20]Department of Developmental Neurobiology, St. Jude Children's Research Hospital, Memphis, TN 48073, USA.

[21]Michigan Center for Translational Pathology, Howard Hughes Medical Institute, University of Michigan, Ann Arbor, MI 48109, USA.

Abstract

High-grade gliomas with arginine or valine substitutions of the histone H3.3 glycine 34 residue (H3.3G34R/V) carry a dismal prognosis, and current treatments, including radiotherapy and chemotherapy, are not curative. Because H3.3G34R/V mutations reprogram epigenetic modifications, we undertook a comprehensive epigenetic approach using ChIP-sequencing and chromHMM computational analysis to define therapeutic dependencies in H3.3G34R/V gliomas. Our analyses revealed a convergence of epigenetic alterations, including: (i) activating epigenetic modifications on histone H3 lysine (K) residues such as H3K36-trimethylation (H3K36me3), H3K27-acetylation (H3K27ac) and H3K4-trimethylation (H3K4me3), (ii) DNA promoter hypomethylation, and (iii) redistribution of repressive histone H3K-trimethylation (H3K27me3) to intergenic regions at the Leukemia Inhibitory Factor (*LIF*) locus to drive increased LIF abundance and secretion by H3.3G34R/V cells. LIF activated Signal Transducer and Activator of Transcription 3 (STAT3) signaling in an autocrine/paracrine manner to promote survival of H3.3G34R/V glioma cells. Moreover, immunohistochemistry and single-cell RNA sequencing from H3.3G34R/V patient tumors revealed high STAT3 protein and RNA expression, respectively, in tumor cells with both inter- and intra-tumor heterogeneity. We targeted STAT3 using a blood-brain barrier penetrable small molecule inhibitor, WP1066, currently in clinical trials for adult gliomas. WP1066 treatment resulted in H3.3G34R/V tumor cell toxicity in vitro and tumor suppression in preclinical animal models established with KNS42 cells, SJ-HGGx42 cells, or in utero electroporation techniques. Our studies identify the LIF/STAT3 pathway as a

key epigenetically-driven and druggable vulnerability in H3.3G34R/V gliomas. This finding could inform development of targeted, combination therapies for these lethal brain tumors.

One Sentence Summary:

Histone H3.3G34R/V mutant gliomas demonstrate LIF/STAT pathway activation that can be disrupted for therapeutic benefit.

Introduction

Brain tumors in children and adolescents are associated with devastating outcomes and have surpassed other tumors as the leading cause of cancer-related death (1). Substantial strides have been made in treating some childhood cancers, such as leukemias, whereas incremental progress has been made for pediatric and adolescent high-grade gliomas (HGGs). The survival rate for HGGs remains dismal with a 5-year patient survival of ~15% (2). No efficacious therapies exist, despite attempts to translate aggressive therapeutic approaches utilized for adult high-grade gliomas to younger patients. Failures of standard therapies have sparked intense focus on understanding the epigenetic and molecular characteristics of HGGs to enable effective treatment discovery.

Research on various pediatric cancers has demonstrated genetic alterations in chromatin remodeling or histone modifying enzymes. Somatic missense mutations in histone proteins have been identified in pediatric brain tumors, soft tissue sarcomas, and bone tumors (3–6). Approximately 30–60% of high-grade gliomas bear mutations in *H3F3A*, the gene encoding histone H3.3 (6). These recurrent mutations involve the replacement of the lysine residue at amino acid 27 by methionine (H3.3K27M) or the glycine residue at amino acid 34 by arginine or valine (H3.3G34R/V). H3.3G34R/V mutations have been observed exclusively in *H3F3A* while H3K27M mutations occur frequently in *H3F3A* and to a lesser extent in *HIST1H3B/C* encoding H3.1. H3K27M tumors are found in midline brain structures and the brainstem of young children, whereas H3.3G34R/V tumors are found in cortical structures of older adolescents and young adults (6). These temporal and anatomical distinctions suggest that distinct molecular programs enable tumorigenesis in specific cellular contexts.

Although our knowledge on the mechanism of action of H3K27M has grown considerably, the molecular mechanisms governing H3.3G34R/V tumorigenesis in gliomas are less claer (7–9). The glycine 34 residue of histone H3.3 is not subject to post-translational modifications, but H3.3G34R/V mutations can impede both the catalytic activity of the H3K36 trimethyltransferase, SET Domain Containing 2 (SETD2), and inhibit H3K36 lysine demethylases KDM4A, KDM4B, and KDM4C to reprogram genomic H3K36me3 distribution (10–15). Similarly, H3.3G34W mutations observed in giant cell tumors can alter genomic H3K36me3 distribution to impact cellular differentiation (3, 16). While H3.3G34 mutations can reprogram genomic H3K36me3, it remains unknown if these epigenetic alterations create therapeutic vulnerabilities. We hypothesized epigenetic alterations in H3K36me3 and other chromatin modifications could identify potential therapeutic targets in H3.3G34R/V HGGs. Here, we show that H3.3G34 mutations epigenetically activate LIF/

STAT3 signaling, presenting an epigenetically driven therapeutic opportunity for treatment of H3G3R/V HGGs.

Results

H3.3G34R/V cells exhibit transcriptomic and epigenetic alterations converging on the LIF/JAK/STAT3 axis

We utilized an integrated epigenomic and transcriptomic approach to understand pathways specifically upregulated by the H3.3G34R mutation. We established isogenic cell lines by expressing hemagglutinin (HA)-tagged H3.3G34R or H3.3WT in immortalized mouse neuronal stem cells (mNSCs). We used previously characterized H3.3K27M expressed in the same mNSCs background (17, 18). We confirmed expression of mutant transgenes in our mNSCs model by Western blotting for HA (fig. S1A). As demonstrated by others, immunoblotting did not exhibit global changes in H3K36me3, H3K4me3, H3K27ac or H3K27me3 between H3.3G34R and H3.3WT or H3.3K27M mNSCs (Fig. 1A) (4). As controls, H3.3K27M mNSCs showed a global decrease in H3K27me3 accompanied by an increase in H3K27ac (Fig. 1A). Although H3.3K27M increased proliferation (18), no major differences in proliferation were noted between H3.3G34R and H3.3WT mNSCs (fig. S1B). We performed RNA sequencing in these cells and determined genes specifically altered in H3.3G34R versus control H3.3WT and H3.3K27M mNSCs, that showed both upregulated (2715) and downregulated (3039) genes (Fig. 1, B and C). Some of the top pathways revealed by gene set enrichment analysis (GSEA) of the 2715 upregulated genes in H3.3G34R mNSCs were related to the JAK/STAT pathway, chemokine, and cytokine signaling (Fig. 1D).

We performed comprehensive analyses of epigenetic modifications in H3.3G34R relative to H3.3WT mNSCs. H3.3G34R/V mutations are known to reduce local H3K36me3 at various genes. However, some genes show a gain of H3K36me3 (10–12, 19, 20). Therefore, we performed H3K36me3 chromatin immunoprecipitation followed by deep sequencing (ChIP-seq) in our isogenic cells (Fig. 1E). Because H3K36me3 in gene bodies is associated with active transcription, we focused on the subset of genes with H3K36me3 enrichment in H3.3G34R versus H3.3WT mNSCs and compared these data with gene expression in H3.3G34R/H3.3WT mNSCs (Fig. 1F). These analyses revealed *Lif* as the top upregulated gene associated with increased H3K36me3 enrichment in H3.3G34R compared to H3.3WT mNSCs (Fig. 1, F and G). *Stat3* did not demonstrate similar H3K36me3 enrichment (fig. S1C). Our finding that the *Lif* locus showed increased H3K36me3 in H3.3G34R mNSCs was validated in additional isogenic H3.3G34R/H3.3WT and H3.3G34W/H3.3WT mouse models developed by Voon *et al.* (2018) and Jain *et al.* (2020), respectively (fig. S1, D and E) (10, 19).

H3K36me3 deposition within gene bodies plays an important role in gene activation and has been reported to cause subsequent changes in transcription-activating H3K27ac and H3K4me3 marks (21–23). ChIP-seq analysis for H3K27ac and H3K4me3 demonstrated overall increased enrichment of these activating marks at promoters in H3.3G34R mNSCs compared to H3.3WT mNSCs (Fig. 1H). GSEA analysis for genes exhibiting promoter H3K27ac elevation revealed pathways associated with cellular responses to Lif (Fig. 1I).

Moreover, H3.3G34R mNSCs demonstrated increased H3K27ac and H3K4me3 enrichment at the *Lif* promoter relative to H3.3WT and H3.3K27M mNSCs (Fig. 1J). Similar analysis of H3K27ac-enriched loci in H3.3WT mNSCs did not reveal pathways associated with Lif signaling (fig. S1F). Interestingly, comparison of H3K27ac ChIP-seq signals from Wang *et al.* (2021) in KNS42 cells with various H3K27M pediatric glioma cells and normal human astrocytes revealed marked enrichment of this mark at *LIF* in KNS42 cells (fig. S1G) (24). Differential changes in H3K36me3, H3K27ac, and H3K4me3 were not observed between mNSCs at other JAK/STAT loci including *Stat3* (fig. S1C). Similarly, no enrichment of H3K36me3 was observed at *Stat3* in other isogenic H3.3G34R/W mouse cells (fig. S1, D and E).

We assessed H3K36me3, H3K27ac, mutant H3.3G34R, mutant H3.3G34V and total H3 at *LIF* in H3.3G34V (KNS42) and H3.3G34R (CHOP-GBM-001 and HSJD-GBM-002) patient-derived cell lines. These results supported findings from H3.3G34R mNSCs and showed enrichment of both H3K36me3 and H3K27ac at the *LIF* locus (Fig. 1K). We noted heterogeneity in the amount of H3.3G34R/V histone present at *LIF* in these patient-derived cell lines. KNS42 and CHOP-GBM-001 cells exhibited higher H3.3G34R/V incorporation compared to HSJD-GBM-002 at the *LIF* locus. Interestingly, the amount of H3.3G34R/V histone, but not total H3, incorporation paralleled the degree of H3K36me3 deposition in the *LIF* gene body (Fig. 1K). Because H3.3G34R/V and H3.3K27M mutations occur in *H3F3A*, we used *H3F3A* mRNA expression as a surrogate for mutant H3.3G34R/V or H3.3K27M expression and assessed its relation to *LIF* expression in patient-derived tumor samples deposited in PedCBioportal by Mackay *et al.* (2017) (25). Each type of pediatric glioma was segregated by histone status and patient samples were sorted by *H3F3A* expression. *H3F3A*-high and *H3F3A*-low categories were defined as tumor with *H3F3A* expression above or below the median expression value, respectively, within a cohort. *LIF* expression was compared between *H3F3A*-high and *H3F3A*-low subclasses, and Pearson correlation analysis was performed to determine relationships with *H3F3A* expression. We noted a positive correlation between *H3F3A* and *LIF* expression in H3.3G34R/V (n=19), but not H3.3K27M (n=71) tumors (fig. S1H). The opposite pattern was observed in H3WT (n=101) tumors (fig. S1H). Additionally, we interrogated H3K36me3 ChIP-seq and RNA-seq data from a study on H3.3G34W mutations in giant cell tumors of the bone by Khazaei *et al.* (2020) (3). Similar to H3.3G34R mNSCs, Im-GCT-4072 patient-derived cells with H3.3G34W mutations showed enrichment of H3K36me3 at *LIF* (fig. S1I). Knockout or correction of mutant H3.3G34W to H3.3WT lowered H3K36me3 enrichment at the *LIF* locus. Importantly, this was associated with decreased *LIF* mRNA compared to controls (fig. S1I) (3).

We also sought to characterize modes of gene regulation by defining chromatin states and their distribution throughout the genome in our isogenic mNSCs. We utilized ChromHMM software (26, 27) to locate where combinations of epigenetic modifications including H3K36me3, H3K4me3, H3K27me3, H3K27ac, H3K4me1 and H3K36me2 were differentially enriched in H3.3G34R relative to H3.3WT and H3.3K27M mNSCs (Fig. 1L). States 6 and 7 were only present in the gene body of *Lif* in H3.3G34R compared to H3.3WT and H3.3K27M mNSCs (Fig. 1L). Additionally, state 1, representing activated transcription, was enriched at *Lif* in H3.3G34R cells relative to H3.3WT and H3.3K27M

mNSCs. State 10, associated with gene repression, was only present at *Lif* in H3.3WT cells (Fig. 1L). Epigenetic state analysis also revealed enrichment of states 6 and 7 (representing H3K36me3 deposition) in H3.3G34R mNSCs, but not in H3.3WT, at genes related to Jak/Stat signaling and cell cycle regulation (Fig. 1M and fig. S1F). Together, these data from epigenetic and transcriptomic analyses in isogenic mNSCs, confirmed in human patient-derived cell lines and tumor samples, suggest that H3.3G34R/V mutations epigenetically upregulate *LIF*.

H3.3G34R/V alters DNA methylation and H3K27me3 at the *LIF* locus.

We evaluated differences in DNA methylation using enhanced reduced representation bisulfite sequencing (ERRBS) in our isogenic mNSCs. Differentially methylated regions (DMRs) were assessed between H3.3G34R versus H3.3WT and H3.3K27M versus H3.3WT cells. We noted a greater proportion of DMRs in H3.3G34R versus H3.3WT mNSCs compared to H3.3K27M versus H3.3WT mNSCs (Fig. 2A). Separate comparisons of H3.3G34R with H3.3WT mNSCs and H3.3K27M with H3.3WT mNSCs demonstrated a greater degree of hypo- and hyper-methylation of CpG-containing promoter regions in H3.3G34R mNSCs (Fig. 2B). We identified many promoters that were hypo- or hyper-methylated in H3.3G34R/H3.3WT but not in H3.3K27M/H3.3WT mNSCs (fig. S2A). Because hypomethylated promoters are associated with increased gene expression, we compared differential promoter methylation with our RNA-seq data (Fig. 2, C and D). Genes with hypomethylated promoters were associated with an overall increase in gene expression in H3.3G34R/H3.3WT mNSCs (Fig. 2C). Although this pattern was similar in H3.3K27M/H3.3WT cells, the degree of difference in gene expression was greater in H3.3G34R/H3.3WT compared to H3.3K27M/H3.3WT mNSCs (fig. S2B). Comparison of hypomethylated promoters with gene expression in H3.3G34R/H3.3WT mNSCs revealed *Lif* as one of the top genes associated with both promoter hypomethylation and increased gene expression (Fig. 2D).

We also assessed the relationship between DNA methylation and genomic distribution of histone marks in H3.3G34R versus H3.3WT mNSCs. Genes with hypomethylated promoters, including *Lif*, exhibited enrichment of activation marks, including H3K36me3 at gene bodies and H3K27ac and H3K4me3 at promoters (Fig. 2, E to G). In contrast, H3K27me3 was lowered at active promoters and increased in the flanking intergenic regions (Fig. 2H). The top genes that showed promoter hypomethylation, enrichment of H3K36me3, H3K27ac and H3K4me3, and increased flanking H3K27me3 included *Lif* and key development and oncogenic factors such as *Emx2*, *Igfbp2*, *Mycn*, *Foxa1*, and *Hoxa1* (Fig. 2I and fig. S2C). Loci with promoter DNA hypermethylation, such as *Lpl*, *Dedd2*, and *Mical1* exhibited opposite trends where lower H3K36me3 deposition in the gene body was associated with lowered H3K27ac and H3K4me3 at promoters relative to H3.3WT mNSCs (fig. S2D), suggesting these histone marks cooperate with DNA methylation to control transcription. Comparison of H3.3K27M and H3.3WT mNSCs did not show similar DNA methylation-associated patterns in H3K36me3, H3K27ac, or H3K4me3 (fig. S2, E to G). Both hypo- and hyper-methylated promoters in H3.3K27M/H3.3WT mNSCs showed lower H3K27ac and higher H3K4me3 and H3K36me3. We extended these findings to human tumors where four out of five CpGi in the *LIF* promoter were hypomethylated in H3.3G34R

(*n*=73) compared to H3.3WT (*n*=1306) glioma samples (Fig. 2, J and K). Overall, these data suggest that H3.3G34R drives increased *Lif* gene expression via epigenetic reprogramming at *Lif* including promoter hypomethylation; enrichment of histone activation marks H3K36me3, H3K27ac and H3K4me3; and reduction of repressive H3K27me3.

H3.3G34R/V mutations drive STAT3 signaling via elevated LIF secretion.

Having established H3.3G34R/V mutations were associated with activating epigenetic modifications at the *Lif* locus, we investigated whether Lif-driven downstream signaling pathways were upregulated. We noted *Lif*, *Jak2*, *Stat3* and downstream transcriptional target *Pim1* were upregulated in H3.3G34R compared to H3.3K27M and H3.3WT mNSCs (Fig. 3A). *Stat5b* was lower in H3.3WT and downregulated in H3.3K27M mNSCs (Fig. 3A). We validated these findings in an independent, *in-utero* electroporation (*IUE*)-based mouse tumor model (28). In this system, plasmids encoding PBase, luciferase, dominant-negative *TP53*, constitutively-active mutant *PDGFRA-D842V*, and WT or G34R *H3F3A* were injected into the lateral ventricle of E13.5 CD-1 mice to induce H3WT or H3.3G34R gliomas. Cultures were established from cells derived from each tumor model. These cell lines termed PPG (mutant TP53, mutant PDGFRA, and mutant G34R H3.3) and PPW (mutant TP53, mutant PDGFRA, and WT H3.3) were subjected to RNA-sequencing. Similar to the results from mNSCs model, analysis of upregulated genes in PPG relative to PPW cells revealed GO and KEGG pathways related to cytokine responses/interactions and Jak/Stat signaling (fig. S3, A to C). We assessed *LIF* mRNA expression in patient-derived, low passage cell lines, finding higher expression in H3.3G34V (KNS42) versus H3.3WT (TS543 and SJ-HGGx39-c) (fig. S3, D and E) and H3.3G34R (SJ-HGGx6-c and SJ-HGGx42-c) versus H3.3WT (SJ-HGGx39-c) cells (fig. S3F).

Because LIF activates STAT3 via phosphorylation, we performed immunoblotting to compare total and phosphorylated Stat3 (pStat3). We found an increase in pStat3 in H3.3G34R compared to both H3.3WT and H3.3K27M mNSCs (Fig. 3B). In patient cell lines, pSTAT3 and STAT3 were higher in H3.3G34V (KNS42) and H3.3G34R (OPGB-GBM-001 and SJ-HGGx42-c) compared to H3.3WT (SF188, UMPed37, and SJGBM2) and H3.3K27M (HSJD-DIPG-007) cells (Fig. 3C and fig. S3G). H3.3G34R/V mutant cells also showed higher JAK2 abundance compared to H3.3WT and H3.3K27M cells (Fig. 3C). We found no upregulation of the AKT pathway, an activator of STAT3, in KNS42 compared to SF188 cells (fig. S3H). We confirmed results from the isogenic mNSCs model in Figure 3B and human cell lines in Figure 3C by establishing additional paired models of H3.3G34R and H3.3WT using SJGBM2, HEK293T, and immortalized human neural stem cells. We observed elevated pSTAT3 in these cells expressing the H3.3G34R transgene independent of the cell type utilized to establish the model (fig. S3, I and J). KNS42 cells also showed increased secretion of LIF into cell culture media compared to H3.3WT (SF188 and UMPed37) cells (Fig. 3D). In parallel, we assessed LIF abundance by immunoblotting in additional H3.3G34R (OPGB-GBM-001 and SJ-HGGx42-c) and H3.3WT (SF188, UMPed37, and SJGBM2) cells (fig. S3K). We noted variation in LIF abundance in H3.3G34R cell lines with lower and higher expression in OPGB-GBM-001 and SJ-HGGx42-c, respectively. This suggests that LIF expression and STAT3 pathway

activation may be heterogeneous across H3.3G34R/V cell lines and patient tissues, mirroring findings from ChIP-seq data presented in Figure 1K.

Elevated LIF abundance has been associated with STAT3 activation and worse prognostic outcomes in malignancy (29). We hypothesized that LIF could regulate STAT3 phosphorylation in H3.3G34 mutant cells. We targeted *LIF* in KNS42 cells with three independent shRNAs, that decreased intracellular (by Western blot, Fig. 3E) and extracellular, supernatant LIF expression (by ELISA, Fig. 3F). Western blotting in these cells revealed decreases in pSTAT3 and total STAT3 on LIF knockdown (Fig. 3G). H3.3G34V KNS42 cells with LIF knockdown exhibited a larger fraction of dead cells compared to parental cells (Fig. 3H). Cell death was abrogated upon addition of recombinant LIF to the culture media (Fig. 3H). Next, we determined if the effects observed with LIF knockdown could be recapitulated by perturbing mutant *H3F3A* expression. We first targeted *H3F3A* in H3.3G34V KNS42 cells with two independent shRNAs. Both shRNA-expressing cells showed lower concentrations of H3.3G34V mutant protein (Fig. 3I). shRNA-mediated knockdown of H3.3G34V decreased both intracellular (by Western blot, Fig. 3J) and secreted (by ELISA, Fig. 3K) LIF in KNS42 cells. We found that shRNA-mediated knockdown of *H3F3A* in H3.3G34R SJ-HGGx42-c cells had a similar effect of decreasing intracellular LIF concentrations (fig. S3L). KNS42 cells with lowered concentrations of mutant H3.3G34V protein showed reduced pSTAT3 and total STAT3 (Fig. 3L), and increased cell death (Fig. 3M) compared to controls. These data from mouse and human tumor cell models suggest that mutant H3.3G34R/V upregulates LIF protein expression, which in turn drives STAT3 activity that is important for the survival of H3.3G34R/V cells.

To corroborate the in vitro findings, we quantified phospho-STAT3 and total STAT3 concentrations in H3.3G34R/V (n=6) and H3.3WT (n=12) high-grade glioma patient tissues described in Table S1 (Fig. 4, A to E). Results demonstrated significantly higher phospho-STAT3 (Fig. 4, B and C; P<0.0001) and total STAT3 (Fig. 4, D and E; P<0.0001) in H3.3G34R/V versus H3.3WT samples. We noted both inter- and intra-tumor heterogeneity in these patient tumors, mirroring data from patient-derived cell lines (Fig. 1K and 3C, and fig. S3J). Next, we queried single cell RNA-seq data from H3.3G34R/V patients presented in Chen *et al.* (2020) and found malignant cells to express *LIFR* (LIF receptor), *JAK2*, and *STAT3* (Fig. 4, F to H). This study found that H3.3G34R/V glioma cells were enriched for both interneuron and astrocytic gene signatures. Our analysis revealed JAK/STAT genes were expressed in cells irrespective of the lineage signature (Fig. 4G). We also noted variations in gene expression within malignant cells derived from the same patient and across patients (fig. S4A).

STAT3 inhibition demonstrates greater toxicity in H3.3G34R/V compared to H3.3WT glioma cells in vitro.

We investigated whether suppression of STAT3 activity had consequences for cell growth. We utilized a CRISPR-Cas9-mediated approach to knockout STAT3 in H3.3G34R/V cells. STAT3 knockout in KNS42 and SJ-HGGx42-c cells resulted in lowered STAT3 concentrations (Fig. 5A and fig. S5A), altered cell growth (Fig. 5B), and lowered

percentage of living cells compared to parental controls (Fig. 5C and fig. S5B). We performed RNA-seq to determine pathways altered on STAT3 knockout (Fig. 5D). GSEA of differentially regulated genes showed deregulated pathways related to immune signatures, cell differentiation and motility, apoptosis, cell death, and neuronal differentiation (Fig. 5D). These results suggest that STAT3 could regulate multiple oncogenic pathways and potentially serve as a therapeutic target for H3.3G34R/V-mutant gliomas.

Given the results from STAT3 knockout experiments, we tested the effect of targeting STAT3 pharmacologically using the well-established selective, small-molecule inhibitor of STAT3 phosphorylation and translocation, Stattic, on mNSCs and human patient-derived cell lines. Treatment of H3.3G34R mNSCs with Stattic resulted in differential cell death compared to that observed in H3.3WT mNSCs (Fig. 5E). We also observed heightened sensitivity to Stattic treatment in H3.3G34V (KNS42) and H3.3G34R (SJ-HGGx6-c and SJHGGx42-c) compared to H3.3WT (SF188, TS543 and SJ-HGGx39-c) and H3.3K27M (HSJD-DIPG-007) (Fig. 5, F and G) cells. STAT3 phosphorylation in KNS42 and SF188 cells decreased in a dose-dependent manner upon treatment with Stattic (Fig. 5H and fig. S5C). We also noted OPGB-GBM-001 cells, an additional H3.3G34R patient-derived model, were sensitive to Stattic (fig. S5D).

We then assessed therapeutic potential of WP1066, a potent, orally bioavailable STAT3 inhibitor with markedly low toxicity in vivo (30, 31). Similar to what we observed with Stattic, WP1066 showed greater toxicity in H3.3G34R compared to H3.3WT mNSCs (Fig. 5I). WP1066 demonstrated greater therapeutic effects in H3.3G34V (KNS42) and H3.3G34R (SJ-HGGx6-c and SJ-HGGx42-c) cells compared to H3.3WT (SF188, TS543, SJ-HGGx39-c) and H3.3K27M (HSJD-DIPG-007) human cell lines (Fig. 5, J and K). Next, we confirmed the sensitivity of OPGB-GBM-001 cells to WP1066 (fig. S5E) and SJ-HGGx42-c to another STAT3 inhibitor, SH-4-54 (fig. S5F). We tested and noted that *IUE*-derived PPG tumor cells grown as explant cultures were sensitive to WP1066 (fig. S5, G and H). Finally, we confirmed differential sensitivity of KNS42 and SF188 cells to WP1066 using bioluminescence-based assay (fig. S5I). Immunoblotting analyses of STAT3 phosphorylation showed dose-dependent decrease in pSTAT3 concentrations in H3.3G34V KNS42, but not in H3.3WT (TS543 and SF188) cells treated with WP1066 (Fig. 5L and fig. S5J).

Inhibition of STAT3 activity is therapeutic in H3.3G34R/V glioma models in vivo.

We then explored the possibility that STAT3 inhibitors have therapeutic potential in preclinical animal models of H3.3G34R/V high-grade gliomas. First, we established a xenograft model by injecting KNS42 cells into the flanks of athymic nude mice. An average tumor volume of 45 mm^3 was observed approximately 8 weeks post-injection at which time Stattic was administered as a proof-of-principle for STAT3 inhibition. Stattic-treated mice had suppressed tumor volumes and showed decreased expression of proliferation marker Ki-67 compared to vehicle-treated animals (fig. S6, A to C). Next, we evaluated the effect of LIF knockdown on tumor growth by injecting KNS42 cells transfected with two independent shRNAs targeting LIF into the flank of athymic nude mice. Approximately 9 weeks after injections, smaller tumor volumes were observed for xenografts with LIF

knockdown with both shRNAs as compared to xenografts without LIF knockdown (fig. S6D).

To corroborate the initial in vivo results, we tested the effect of *STAT3* knockout on tumor growth in an orthotopic model. KNS42 cells with or without *STAT3* knockout (KO) were implanted in the cortex of NSG mice. Tumor progression was monitored via measurement of bioluminescence signal by in vivo imaging systems (IVIS) and Kaplan-Meier analyses were performed. Mice with tumors harboring *STAT3* KO tumors had significantly increased overall survival (Fig. 6A; P=0.0142). KNS42 cells formed aggressive tumors with evidence of tumor invasion into the surrounding skull in control animals. In contrast, a smaller fraction of mice with *STAT3* KO tumors exhibited skull invasion (Fig. 6B). These mice demonstrated lower tumor burden compared to controls, assessed as fold change in bioluminescent signal relative to baseline (Fig. 6C). Next, we investigated pharmacological targeting of STAT3 using several orthotopic models. Although various STAT3 inhibitors have been synthesized, the ability to deliver these drugs to the brain remains largely unknown due to lack of in-depth pharmacokinetic and bioavailability studies. To address this difficulty, we utilized the BOILED-Egg (Brain Or Intestinal EstimateD permeation) model that considers both lipophilicity and polarity chemical parameters to predict absorption, distribution, metabolism, and excretion (ADME) properties for compounds (32). We analyzed the predicted blood-brain barrier (BBB) penetrability of 45 small molecule STAT3 inhibitors (32) (Fig. 6D). We filtered for STAT3 inhibitors currently in clinical trials. From these analyses, WP1066 was the only compound with predicted favorable ADME parameters including high BBB-penetrability that also showed efficacy in preclinical glioblastoma models (31, 33) and is currently in clinical trials for malignant gliomas and CNS metastatic melanomas (NCT01904123, NCT04334863) (Fig. 6D). In contrast, Stattic exhibited unfavorable absorption and poor BBB-penetration (Fig. 6D). Based on these results, we tested efficacy of WP1066 in four independent H3.3G34R/V glioma animal models.

In the first model, we utilized an *in-utero* electroporation-based H3.3G34R PPG tumor model (H3.3G34R *IUE*) established in CD-1 mice to study WP1066 efficacy. Successful tumor engraftment was confirmed by capturing bioluminescent signal via IVIS. WP1066 was administered once per day (Monday through Friday) at 40 mg/kg for 6 weeks [based on published doses (33)] as outlined in Figure 6E. WP1066-treated mice had significantly increased overall survival compared with vehicle-treated controls (Fig. 6F; P<0.0058). Furthermore, mice receiving WP1066 had significantly lower tumor burden compared to vehicle-treated animals, assessed as fold change in bioluminescent signal relative to baseline (Fig. 6, G and H; P<0.0173). Next, we established a human H3.3G34V tumor model by orthotopically implanting mice with KNS42 cells in the cortex and confirmed engraftment via IVIS. Using the same treatment paradigm (Fig. 6E), mice receiving WP1066 exhibited significantly prolonged survival (P<0.0019) and decreased tumor burden (P<0.0222) compared to vehicle-treated control animals (Fig. 6, I to K). Neuropathological features were assessed in tumors with or without treatment. All mice with KNS42 tumors receiving vehicle exhibited tumor invasion into the surrounding skull while less than 50% of WP1066-treated mice demonstrated this phenotype (Fig. 6L). Moreover, Ki-67 expression was reduced in mice receiving WP1066 (Fig. 6M) compared to vehicle-treated animals. In

contrast, WP1066 treatment of a H3.3WT glioma orthotopic model developed with TS543 cells did not result in decreased tumor burden (Figure S6, E and F). We further confirmed our results in NSG mice orthotopically implanted with H3.3G34R PPG and SJ-HGGx42-c cells. As observed during in vitro studies, WP1066 treatment resulted in lower tumor burden (as determined by IVIS bioluminescence) in both models (fig. S6, G to L) and extended overall survival in mice with orthotopic PPG tumors (fig. S6H).

Last, we investigated the possibility that H3.3G34R/V tumors may benefit from treatment comprised of current standard radiation therapy (RT) paired with STAT3 inhibitors. Constitutive STAT3 activation has been implicated in tumor radioresistance, and consequently, recent studies have attempted to target STAT proteins to promote radiosensitivity (34, 35). We used orthotopic models of H3.3G34R PPG, SJ-HGGx42-c, and KNS42 cells established in NSG mice. Potential synergy between radiation therapy and WP1066 was assessed using a modified treatment paradigm (fig. S6G). Both RT and combination therapy extended overall survival in H3.3G34R PPG animals. Combination therapy significantly extended overall survival compared to radiation therapy alone (fig. S6H; P=0.0004). However, combination therapy provided no additional benefit compared to single agent WP1066 treatment (fig. S6H). RT alone, or combination treatment, markedly lowered tumor burden (as determined by IVIS bioluminescence) in H3.3G34R PPG, but not in SJ-HGGx42 or KNS42 engrafted animals (fig. S6, I to O). A significant decrease in tumor signal was only noted in WP1066-treated SJ-HGGx42 tumor-bearing mice, but not after other treatment modes (fig. S6L; P=0.0105). Studies of irradiation of brain and other solid tumors has revealed that irradiation itself can enhance STAT3 signaling (24, 34, 36). We therefore hypothesized that this mechanism could account for the resistance of SJ-HGGx42 tumors to RT. SJ-HGGx42-c cells subjected to a single dose of radiation with or without STAT3 inhibitor in vitro demonstrated that irradiation enhanced phospho-STAT3 and total STAT3 concentrations (fig. S6M). This enhancement of STAT3 signaling potentially explains why no additive effect of the combination regimen was observed in vivo. Similarly, treatment of KNS42 orthotopic tumors did not result in a consistently decreased tumor signal and, like controls, the skull invasion phenotype was observed in RT-treated mice (fig. S6, N and O). Together our results in vitro and in vivo serve as proof-of-principle that reducing STAT3 activity with the BBB-penetrable WP1066 is therapeutic in preclinical H3.3G34R/V glioma models.

Discussion

The discovery of histone mutations in glioma has expanded knowledge on how these mutations alter chromatin to impact tumor pathogenesis. Here, we defined therapeutic dependencies arising from epigenetic alterations in H3.3G34R/V glioma. Using cell-based epigenetic and transcriptomic approaches, we discovered that H3.3G34R/V cells demonstrate enhanced LIF/STAT3 signaling compared to H3.3WT cells. This finding was corroborated by single-cell RNA-seq and immunohistochemical analysis of H3.3G34R/V patient cells and tumor tissues. We noted inter- and intra-tumor heterogeneity in LIF receptor, LIF, and pSTAT3/STAT3 abundances in these cells and tissues, suggesting a subset of H3.3G34R/V glioma patients may benefit from STAT3-targeting therapies.

Mechanistically, H3.3G34 mutant-expressing cells showed enrichment of multiple activating marks, including H3K36me3, at *LIF* to drive LIF expression, and knockdown of mutant *H3F3A* lowered LIF protein expression and secretion. Recent studies have shown that H3.3G34R/V/W mutant cells demonstrate both genome-wide gains and losses of H3K36me3 (10–12, 19, 20). Regions with loss of H3K36me3 include genes related to differentiation (3). Our data from mouse and human tumor cell models suggest that regions gaining H3K36me3 involve genes related to the LIF/JAK/STAT pathway.

Pediatric high-grade gliomas harboring H3.3G34R/V or H3.1/H3.3K27M mutations often occur with other mutations in cancer-associated genes such as *TP53, PDGFRA, EGFR*, and *ATRX/DAXX (25, 37)*. These genes can independently or collectively alter cellular signaling and metabolism, leading to difficulty in isolating specific effects of mutant histones. Single cell-sequencing studies on H3.3G34R/V tumors have revealed stem-like interneuron progenitors as potential cells of origin (37). Furthermore, recent studies have utilized forebrain neuronal stem cells or progenitor cells to model H3.3G34R/V tumors (38, 39). Thus, our in vitro isogenic models developed with mouse-derived cortical neuronal stem cells (mNSCs) avoid potential confounds from co-occurring mutations.

In this study, we noted H3.3G34R mNSCs exhibit a distinct DNA methylation profile and harbor more differentially methylated regions than H3K27M cells when compared with H3WT cells. These findings recapitulate observations by Sturm *et al*. (2012) and Sangatsuda *et al*. (2020) who reported robust changes occur in DNA methylation in H3.3G34R/V versus H3 wild-type tumors, but to a lesser extent in H3.3K27M tumors (6, 16). Promoter hypomethylation in H3.3G34R-expressing mNSCs was associated with increased gene expression and enrichment of transcription-activating epigenetic marks including H3K36me3, H3K27ac and H3K4me3 in H3.3G34R mNSCs. We observed H3K36me3 gain at DNA hypomethylated loci but did not observe decreases in H3K36me3 to a similar extent at hypermethylated loci. Moreover, H3K27me3 was redistributed with lowered H3K27me3 at promoter regions and increased H3K27me3 in flanking intergenic regions, mirroring findings reported in H3.3G34W bone tumor cells (3). Cross referencing epigenetic alterations with DNA methylation revealed *Lif* as a top upregulated gene. In addition, we observed H3K36me3 gain and promoter hypomethylation at *Mycn*, mirroring findings of Bjerke *et al*. (2013) who reported H3K36me3 gain at *MYCN* in H3.3G34V KNS42 cells (11). Taken together, results from both studies suggest that perturbation of promoter methylation by H3.3G34R/V promotes oncogenic gene activation. Altogether, our findings of H3.3G34R/V deposition at *LIF* in patient-derived cells, promoter hypomethylation in our isogenic model and patient samples, and epigenetic upregulation of LIF in both G34W and G34R/V tumors strongly suggest a key role for LIF in pathogenesis of H3.3G34R/V mutant gliomas.

H3.3G34R/V tumor-specific mechanisms causing DNA methylation changes remain unknown. Interestingly, DNA methyltransferase DNMT3A has been shown to recognize and interact with H3K36me3 via a critical PWWP domain (40). Our results suggest the hypothesis that H3.3G34R/V histones may inhibit DNMT3 activity or block their recognition of H3K36me3, resulting in hypomethylation of promoters with high mutant histone incorporation. To dissect this, future studies could perform additional ChIP-

seq and histone association assays to understand the genomic localization of DNA methyltransferases and demethylases and their patterning relative to the H3.3G34R/V histone distribution. It is also quite possible that H3.3G34R/V histones do not directly interact with DNMT3 proteins and DNA hypomethylation is a secondary effect. Importantly, H3K4me3 enrichment can antagonize DNA methylation by blocking the interaction of DNMT3 proteins with unmodified H3K4 residues (41). We have noted loci with concomitant H3K36me3 and H3K4me3 gain in H3.3G34R cells, suggesting the possibility that H3.3G34-mutant histones bind lysine 4 demethylases of the KDM5 family, causing H3K4me3 accumulation via a similar mechanism observed for lysine 36 demethylases (10), and subsequent DNMT3 antagonism. Overall, our findings highlight the need to better understand how mutant histones interfere with DNA methylation molecular machinery.

Functional studies demonstrated that LIF activated STAT3 signaling in an autocrine/paracrine manner and was important for cell survival of H3.3G34R/V mutant cells, suggesting a key epigenetically-driven therapeutic vulnerability. STAT proteins serve as master transcriptional regulators and their dysregulation or overexpression has been noted widely in malignancy (42), prompting substantial efforts to find suitable inhibitors. Obstacles in developing STAT3 inhibitors for gliomas include rapid clearance and low blood-brain barrier penetrability. Here, we took advantage of low toxicity and high brain penetrability of a promising small molecule STAT3 inhibitor WP1066 (30, 33). WP1066 treatment resulted in marked tumor toxicity in H3.3G34R/V models both in vitro and in vivo. Although radiation was able to decrease tumor burden and increase survival in one H3.3G34R orthotopic tumor model, combining radiation with WP1066 in vivo did not enhance the survival benefit of WP1066 treatment alone. Our results suggest a key epigenetically-driven vulnerability in H3.3G34R/V mutant gliomas that can be leveraged for therapeutic purposes using established STAT3 inhibitors. Moreover, the ability of H3.3G34R/V/W mutations to modulate epigenetic modifications at *LIF* and its expression provide support to other studies which have suggested H3.3G34R and H3.3G34W work via similar mechanisms and thus could both benefit from STAT3 inhibition.

Intriguingly, a recent study profiling the mutational landscape of H3.3G34R/V tumors noted a large frequency of co-occurring *PDGFRA* mutations (37). The authors found that aberrant PDGFRA activation also correlated with MEK/ERK pathway activation in H3.3G34R/V patient tumors. Interestingly, studies have demonstrated that platelet derived growth factor (PDGFR) can activate JAK/STAT signaling (43). Other work has uncovered the role of ERK1/2 in phosphorylating the STAT3 serine 727 residue (44). S727 activation has varying roles depending on cell type and has been associated with enhanced STAT3 DNA binding and radioresistance mechanisms (45). These findings suggest that MEK/ERK activation in H3.3G34-mutant tumors might confer resistance to STAT3 therapies. Because the S727 residue cannot be pharmacologically targeted like Y705, H3.3G34R/V tumors may benefit from combined MEK/ERK and STAT3 signaling inhibition. Furthermore, studies have revealed that WP1066 can effectively decrease ERK1/2 phosphorylation (46). These unique properties make WP1066 an ideal candidate for clinical testing where therapy may simultaneously target STAT3 and ERK1/2 signaling.

Limitations of this study include the small number of isogenic model cells and patient-derived cell lines and tissues. Only recently have new patient-derived cell cultures been established to study H3.3G34R/V-specific molecular mechanisms and profile epigenetic changes with ChIP-sequencing. Few studies have established in vivo models which reflects the limited models available in this field. Overall, our study furthers knowledge about H3.3G34R/V biology by uncovering a H3.3G34-driven epigenetic mechanism for LIF/STAT3 activation. However, we noted heterogeneity in STAT3 activation across tumor samples and cells, suggesting that STAT3 therapy may not be as effective in some patients. Further, some samples demonstrated elevated STAT3 activity in a LIF-independent manner, suggesting other mechanisms might activate STAT3 in a subset of tumors and necessitating additional study. We successfully established several mouse xenograft models of H3.3G34R/V glioma which revealed STAT3-targeting as an effective therapeutic axis. Importantly, WP1066 is BBB-penetrable and is currently in clinical trials for malignant gliomas and CNS metastatic melanomas (NCT01904123, NCT04334863). Collectively, this work highlights a potential therapeutic lead for the treatment of H3.3G34R/V gliomas.

Materials and Methods

Study Design

This study focused on assessing specific epigenetic, transcriptomic, and proteomic changes in H3.3G34R/V tumors and explored whether signaling mechanisms activated by H3.3G34R/V mutations provide therapeutic vulnerabilities in these tumors. We first used H3.3G34R/V mouse and human tumor model cells to delineate epigenetic patterns and profile signaling pathways. We observed increases in H3K36me3 at the *LIF* locus in these models which led us to hypothesize that H3K36me3 drives other epigenetic changes at *LIF* that promotes its expression and drives STAT3 signaling in these tumors. Genetic and pharmacological approaches were utilized to probe STAT3 as a potential therapeutic target in isogenic model cells and patient-derived tumor cells. Finally, we demonstrated that STAT3 is a viable, translational therapeutic target in H3.3G34R/V tumors using multiple mouse tumor models.

In vitro pharmacology, qPCR, immunoblotting, and ELISAs were performed using three independent experiments with technical replicates (n=3–4 or greater) of each condition. DNA methylation and RNA-seq analysis was performed in triplicate for each cell line or assay condition. ChIP-seq analysis was conducted using n=1 biological replicate for each epigenetic modification using isogenic H3.3G34R, H3.3WT or H3.3K27M mutant cells or human pHGG glioma cells. Both mouse histone mutant cells and patient-derived high-grade glioma cell lines were utilized for in vitro experiments. No data was excluded from any in vitro analysis.

All animal experiments were performed after approval from the University of Michigan Institutional Animal Care and Use Committee (Protocols #8865 and #9398) and were conducted as per NIH guidelines for animal welfare. Both male and female mice were equally used. Flank and orthotopic murine models of H3.3G34R/V tumors were established via either injection of target cells or *in-utero* electroporation techniques (18, 28). Sample sizes for in vivo animal experiments were based on previously published in vivo pHGG

models by Grasso *et al.* (2015) which showed a minimum group size of three animals to detect a 50% difference in tumor growth between two groups with an alpha=0.05 and power=0.8 (47). For subcutaneous models, treatment and measurements began at 8 weeks post-injection when control tumors measured approximately 45 mm^3. For TS543, SJ-HGGx42-c, PPG and H3.3G34R *IUE* orthotopic models, treatment was commenced 10–12 days after tumor cell implantation and tumors were imaged weekly. For the orthotopic model of KNS42 *STAT3* KO tumors, bioluminescence measurements were obtained weekly beginning 10 days post-implantation. For the orthotopic model of KNS42 tumors receiving WP1066, treatment was commenced 7 weeks after tumor cell implantation and tumors were imaged weekly. For all studies, engraftment of tumors in the cortex was confirmed by bioluminescence imaging (IVIS). Animals with failed tumor engrafting (absence of bioluminescence signal or bioluminescence did not reach a predefined threshold) were not included for further study. At treatment commencement, total flux exceeded the following predetermined threshold (>10^6 photons/sec for KNS42, H3.3G34R-*IUE*, H3.3G34R-PPG, and TS543 models; >10^5 photons/sec for the SJ-HGGx42 model).

After confirmation of appropriate tumor formation, mice were randomized into control and experimental groups before Stattic or WP1066 treatment, radiotherapy, or combinatorial treatment. Tumor progression was evaluated weekly by measuring tumor dimensions or assessing bioluminescence signal longitudinally by IVIS in a non-blinded manner. Mice were sacrificed at a humane endpoint (i.e. onset of neurologic symptoms, lethargy, or lack of ambulation). Immunostaining for in vivo studies and patient samples was performed by capturing and performing quantification analyses by individuals blinded to the experimental design or sample type. All identifiers from cases were removed before analysis. A priori power analysis was not conducted to determine sample size for methylation or expression data derived from patient samples. Sample size for these analyses was determined based on tumor specimen availability. All studies were conducted in compliance with REMARK and STARD guidelines.

Statistical Analyses

Statistical analyses were performed in consultation with bioinformaticians. The sample size (n) along with the statistical test performed and corresponding P-values are indicated in each figure and figure legend. Data in all figures is represented as the mean ± standard deviation (S.D.) unless otherwise indicated. Graphs were plotted and statistical analyses were performed using Prism software (Version 8.0.0, Windows 64-bit, GraphPad, La Jolla, CA). Unpaired, two-sided, two-tailed, Student's t test or two-sided analysis of variance (ANOVA) followed by multiple comparison analysis were used to analyze data as indicated. Correlational analyses were performed using 95% confidence intervals. Results from correlational analyses are represented by r, Pearson's correlation coefficient. Survival analyses for animal experiments was performed using Kaplan-Meier analyses utilizing the Log-Rank test. Data were considered significant if $P < 0.05$.

Supplementary Material

Refer to Web version on PubMed Central for supplementary material.

Acknowledgments:

We would like to thank P. Mukherjee from the Epigenetics Core Facility at Weill Medical College of Cornell University for assistance with DNA methylation experiments. We would like to thank the Chad Carr Foundation (Tammi and Jason Carr) and the University of Michigan Chad Carr Pediatric Brain Tumor Initiative.

Funding:

The Venneti Laboratory was/is supported by the Mathew Larson (to SV), St Baldrick's (to SV), Claire McKenna (to SV), Alex Lemonade Stand (to SV), Storm The Heavens (to SV), Hyundai Hope on Wheels (to SV), Michael Mosier Defeat DIPG (to CC), ChadTough (to CC, SV), Robert Connor Dawes/National Brain Tumor Society/ Ependymoma Cancer Research Network (to CC), Sidney Kimmel (to SV), Doris Duke (to SV) and Sontag Foundations (to SV). The Venneti Laboratory is also supported by grants from NCI R01 NS110572 (to SV). CC acknowledges support from the DGIST Start-up Fund Program of the Ministry of Science and ICT (grant #2021050001 to CC). CJK acknowledges support from NIH/NINDS (K08-NS099427-01 to CJK). SJB acknowledges funding from NIH (CA096832 to SJB). AS, VR and AR were partially supported by NCI grant R37-CA214955 (to AR), The University of Michigan (U-M) institutional research funds, and also supported by ACS grant RSG-16-005-01 (to AR). AJS acknowledges support from NIH/NCI grants (F32CA260735 to AJS, and T32CA009676 to AJS). DRW receives funding from the NCI (K08CA234416 to DRW, and R37CA258346 to DRW), the Damon Runyon Cancer Research Foundation and the Ben and Catherine Ivy Foundation.

Data and materials availability:

All data associated with this study are in the paper or supplementary materials. OPGB-GBM-001 cells were obtained after MTA from M. Vinci (Department of Hematology/ Oncology, Bambino Gesu Children's Hospital-IRCCS, Rome, Italy). SJ-HGGx6-c, SJ-HGGx42-c, SJ-HGGx37-c, and SJ-HGGx39-c were obtained after MTA from S. Baker (Department of Developmental Neurobiology, St. Jude Children's Research Hospital, Memphis, TN, USA). mNSCs were obtained after MTA from R.J. Gilbertson (St. Jude Children's Research Hospital, Memphis, TN, USA). HA-tagged H3.3G34R, H3.3K27M, and H3.3WT expression plasmids were obtained from C. David Allis. hNSCs were obtained after MTA from E. Raabe (Johns Hopkins University School of Medicine, Baltimore, MD, USA). H3K36me3, H3K4me3, H3K27ac, and H3K27me3 ChIP-seq raw data have been deposited in the NCBI Gene Expression Omnibus (GEO#). RNA-seq and DNA methylation raw data have been deposited in the NCBI Gene Expression Omnibus (GEO #).

References

1. Jones C, Karajannis MA, Jones DTW, Kieran MW, Monje M, Baker SJ, Becher OJ, Cho YJ, Gupta N, Hawkins C, Hargrave D, Haas-Kogan DA, Jabado N, Li XN, Mueller S, Nicolaides T, Packer RJ, Persson AI, Phillips JJ, Simonds EF, Stafford JM, Tang Y, Pfister SM, Weiss WA, Pediatric high-grade glioma: biologically and clinically in need of new thinking. Neuro Oncol 19, 153–161 (2017). [PubMed: 27282398]
2. Louis DN, Perry A, Wesseling P, Brat DJ, Cree IA, Figarella-Branger D, Hawkins C, Ng HK, Pfister SM, Reifenberger G, Soffietti R, von Deimling A, Ellison DW, The 2021 WHO Classification of Tumors of the Central Nervous System: a summary. Neuro Oncol, (2021).
3. Khazaei S, De Jay N, Deshmukh S, Hendrikse LD, Jawhar W, Chen CC, Mikael LG, Faury D, Marchione DM, Lanoix J, Bonneil E, Ishii T, Jain SU, Rossokhata K, Sihota TS, Eveleigh R, Lisi V, Harutyunyan AS, Jung S, Karamchandani J, Dickson BC, Turcotte R, Wunder JS, Thibault P, Lewis PW, Garcia BA, Mack SC, Taylor MD, Garzia L, Kleinman CL, Jabado N, H3.3G34W promotes growth and impedes differentiation of osteoblast-like mesenchymal progenitors in Giant Cell Tumour of Bone. Cancer Discov, (2020).
4. Lewis PW, Muller MM, Koletsky MS, Cordero F, Lin S, Banaszynski LA, Garcia BA, Muir TW, Becher OJ, Allis CD, Inhibition of PRC2 activity by a gain-of-function H3 mutation found in pediatric glioblastoma. Science 340, 857–861 (2013). [PubMed: 23539183]

5. Lu C, Jain SU, Hoelper D, Bechet D, Molden RC, Ran L, Murphy D, Venneti S, Hameed M, Pawel BR, Wunder JS, Dickson BC, Lundgren SM, Jani KS, De Jay N, Papillon-Cavanagh S, Andrulis IL, Sawyer SL, Grynspan D, Turcotte RE, Nadaf J, Fahiminiyah S, Muir TW, Majewski J, Thompson CB, Chi P, Garcia BA, Allis CD, Jabado N, Lewis PW, Histone H3K36 mutations promote sarcomagenesis through altered histone methylation landscape. Science 352, 844–849 (2016). [PubMed: 27174990]

6. Sturm D, Witt H, Hovestadt V, Khuong-Quang DA, Jones DT, Konermann C, Pfaff E, Tonjes M, Sill M, Bender S, Kool M, Zapatka M, Becker N, Zucknick M, Hielscher T, Liu XY, Fontebasso AM, Ryzhova M, Albrecht S, Jacob K, Wolter M, Ebinger M, Schuhmann MU, van Meter T, Fruhwald MC, Hauch H, Pekrun A, Radlwimmer B, Niehues T, von Komorowski G, Durken M, Kulozik AE, Madden J, Donson A, Foreman NK, Drissi R, Fouladi M, Scheurlen W, von Deimling A, Monoranu C, Roggendorf W, Herold-Mende C, Unterberg A, Kramm CM, Felsberg J, Hartmann C, Wiestler B, Wick W, Milde T, Witt O, Lindroth AM, Schwartzentruber J, Faury D, Fleming A, Zakrzewska M, Liberski PP, Zakrzewski K, Hauser P, Garami M, Klekner A, Bognar L, Morrissy S, Cavalli F, Taylor MD, van Sluis P, Koster J, Versteeg R, Volckmann R, Mikkelsen T, Aldape K, Reifenberger G, Collins VP, Majewski J, Korshunov A, Lichter P, Plass C, Jabado N, Pfister SM, Hotspot mutations in H3F3A and IDH1 define distinct epigenetic and biological subgroups of glioblastoma. Cancer Cell 22, 425–437 (2012). [PubMed: 23079654]

7. Bender S, Tang Y, Lindroth AM, Hovestadt V, Jones DT, Kool M, Zapatka M, Northcott PA, Sturm D, Wang W, Radlwimmer B, Hojfeldt JW, Truffaux N, Castel D, Schubert S, Ryzhova M, Seker-Cin H, Gronych J, Johann PD, Stark S, Meyer J, Milde T, Schuhmann M, Ebinger M, Monoranu CM, Ponnuswami A, Chen S, Jones C, Witt O, Collins VP, von Deimling A, Jabado N, Puget S, Grill J, Helin K, Korshunov A, Lichter P, Monje M, Plass C, Cho YJ, Pfister SM, Reduced H3K27me3 and DNA hypomethylation are major drivers of gene expression in K27M mutant pediatric high-grade gliomas. Cancer Cell 24, 660–672 (2013). [PubMed: 24183680]

8. Harutyunyan AS, Krug B, Chen H, Papillon-Cavanagh S, Zeinieh M, De Jay N, Deshmukh S, Chen CCL, Belle J, Mikael LG, Marchione DM, Li R, Nikbakht H, Hu B, Cagnone G, Cheung WA, Mohammadnia A, Bechet D, Faury D, McConechy MK, Pathania M, Jain SU, Ellezam B, Weil AG, Montpetit A, Salomoni P, Pastinen T, Lu C, Lewis PW, Garcia BA, Kleinman CL, Jabado N, Majewski J, H3K27M induces defective chromatin spread of PRC2-mediated repressive H3K27me2/me3 and is essential for glioma tumorigenesis. Nat Commun 10, 1262 (2019). [PubMed: 30890717]

9. Larson JD, Kasper LH, Paugh BS, Jin H, Wu G, Kwon CH, Fan Y, Shaw TI, Silveira AB, Qu C, Xu R, Zhu X, Zhang J, Russell HR, Peters JL, Finkelstein D, Xu B, Lin T, Tinkle CL, Patay Z, Onar-Thomas A, Pounds SB, McKinnon PJ, Ellison DW, Zhang J, Baker SJ, Histone H3.3 K27M Accelerates Spontaneous Brainstem Glioma and Drives Restricted Changes in Bivalent Gene Expression. Cancer Cell 35, 140–155 e147 (2019). [PubMed: 30595505]

10. Voon HPJ, Udugama M, Lin W, Hii L, Law RHP, Steer DL, Das PP, Mann JR, Wong LH, Inhibition of a K9/K36 demethylase by an H3.3 point mutation found in paediatric glioblastoma. Nat Commun 9, 3142 (2018). [PubMed: 30087349]

11. Bjerke L, Mackay A, Nandhabalan M, Burford A, Jury A, Popov S, Bax DA, Carvalho D, Taylor KR, Vinci M, Bajrami I, McGonnell IM, Lord CJ, Reis RM, Hargrave D, Ashworth A, Workman P, Jones C, Histone H3.3. mutations drive pediatric glioblastoma through upregulation of MYCN. Cancer Discov 3, 512–519 (2013). [PubMed: 23539269]

12. Fang J, Huang Y, Mao G, Yang S, Rennert G, Gu L, Li H, Li GM, Cancer-driving H3.3G34V/R/D mutations block H3K36 methylation and H3K36me3-MutSalpha interaction. Proc Natl Acad Sci U S A 115, 9598–9603 (2018). [PubMed: 30181289]

13. Shi L, Shi J, Shi X, Li W, Wen H, Histone H3.3 G34 Mutations Alter Histone H3K36 and H3K27 Methylation In Cis. J Mol Biol 430, 1562–1565 (2018). [PubMed: 29689253]

14. Yang S, Zheng X, Lu C, Li GM, Allis CD, Li H, Molecular basis for oncohistone H3 recognition by SETD2 methyltransferase. Genes Dev 30, 1611–1616 (2016). [PubMed: 27474439]

15. Zhang Y, Shan CM, Wang J, Bao K, Tong L, Jia S, Molecular basis for the role of oncogenic histone mutations in modulating H3K36 methylation. Sci Rep 7, 43906 (2017).

16. Sangatsuda Y, Miura F, Araki H, Mizoguchi M, Hata N, Kuga D, Hatae R, Akagi Y, Amemiya T, Fujioka Y, Arai Y, Yoshida A, Shibata T, Yoshimoto K, Iihara K, Ito T, Base-resolution

methylomes of gliomas bearing histone H3.3 mutations reveal a G34 mutant-specific signature shared with bone tumors. Sci Rep 10, 16162 (2020).

17. Johnson RA, Wright KD, Poppleton H, Mohankumar KM, Finkelstein D, Pounds SB, Rand V, Leary SE, White E, Eden C, Hogg T, Northcott P, Mack S, Neale G, Wang YD, Coyle B, Atkinson J, DeWire M, Kranenburg TA, Gillespie Y, Allen JC, Merchant T, Boop FA, Sanford RA, Gajjar A, Ellison DW, Taylor MD, Grundy RG, Gilbertson RJ, Cross-species genomics matches driver mutations and cell compartments to model ependymoma. Nature 466, 632–636 (2010). [PubMed: 20639864]
18. Chung C, Sweha SR, Pratt D, Tamrazi B, Panwalkar P, Banda A, Bayliss J, Hawes D, Yang F, Lee HJ, Shan M, Cieslik M, Qin T, Werner CK, Wahl DR, Lyssiotis CA, Bian Z, Shotwell JB, Yadav VN, Koschmann C, Chinnaiyan AM, Bluml S, Judkins AR, Venneti S, Integrated Metabolic and Epigenomic Reprograming by H3K27M Mutations in Diffuse Intrinsic Pontine Gliomas. Cancer Cell 38, 334–349 e339 (2020). [PubMed: 32795401]
19. Jain SU, Khazaei S, Marchione DM, Lundgren SM, Wang X, Weinberg DN, Deshmukh S, Juretic N, Lu C, Allis CD, Garcia BA, Jabado N, Lewis PW, Histone H3.3 G34 mutations promote aberrant PRC2 activity and drive tumor progression. Proc Natl Acad Sci U S A, (2020).
20. Jiao F, Li Z, He C, Xu W, Yang G, Liu T, Shen H, Cai J, Anastas JN, Mao Y, Yu Y, Lan F, Shi YG, Jones C, Xu Y, Baker SJ, Shi Y, Guo R, RACK7 recognizes H3.3G34R mutation to suppress expression of MHC class II complex components and their delivery pathway in pediatric glioblastoma. Sci Adv 6, eaba2113 (2020).
21. Morris SA, Shibata Y, Noma K, Tsukamoto Y, Warren E, Temple B, Grewal SI, Strahl BD, Histone H3 K36 methylation is associated with transcription elongation in Schizosaccharomyces pombe. Eukaryot Cell 4, 1446–1454 (2005). [PubMed: 16087749]
22. Yuan W, Xu M, Huang C, Liu N, Chen S, Zhu B, H3K36 methylation antagonizes PRC2-mediated H3K27 methylation. J Biol Chem 286, 7983–7989 (2011). [PubMed: 21239496]
23. Venkatesh S, Smolle M, Li H, Gogol MM, Saint M, Kumar S, Natarajan K, Workman JL, Set2 methylation of histone H3 lysine 36 suppresses histone exchange on transcribed genes. Nature 489, 452–455 (2012). [PubMed: 22914091]
24. Wang J, Huang TY, Hou Y, Bartom E, Lu X, Shilatifard A, Yue F, Saratsis A, Epigenomic landscape and 3D genome structure in pediatric high-grade glioma. Sci Adv 7, (2021).
25. Mackay A, Burford A, Carvalho D, Izquierdo E, Fazal-Salom J, Taylor KR, Bjerke L, Clarke M, Vinci M, Nandhabalan M, Temelso S, Popov S, Molinari V, Raman P, Waanders AJ, Han HJ, Gupta S, Marshall L, Zacharoulis S, Vaidya S, Mandeville HC, Bridges LR, Martin AJ, Al-Sarraj S, Chandler C, Ng HK, Li X, Mu K, Trabelsi S, Brahim DH, Kisljakov AN, Konovalov DM, Moore AS, Carcaboso AM, Sunol M, de Torres C, Cruz O, Mora J, Shats LI, Stavale JN, Bidinotto LT, Reis RM, Entz-Werle N, Farrell M, Cryan J, Crimmins D, Caird J, Pears J, Monje M, Debily MA, Castel D, Grill J, Hawkins C, Nikbakht H, Jabado N, Baker SJ, Pfister SM, Jones DTW, Fouladi M, von Bueren AO, Baudis M, Resnick A, Jones C, Integrated Molecular Meta-Analysis of 1,000 Pediatric High-Grade and Diffuse Intrinsic Pontine Glioma. Cancer Cell 32, 520–537 e525 (2017). [PubMed: 28966033]
26. Ernst J, Kellis M, ChromHMM: automating chromatin-state discovery and characterization. Nat Methods 9, 215–216 (2012). [PubMed: 22373907]
27. Ernst J, Kellis M, Chromatin-state discovery and genome annotation with ChromHMM. Nat Protoc 12, 2478–2492 (2017). [PubMed: 29120462]
28. Patel SK, Hartley RM, Wei X, Furnish R, Escobar-Riquelme F, Bear H, Choi K, Fuller C, Phoenix TN, Generation of diffuse intrinsic pontine glioma mouse models by brainstem-targeted in utero electroporation. Neuro Oncol 22, 381–392 (2020). [PubMed: 31638150]
29. McLean K, Tan L, Bolland DE, Coffman LG, Peterson LF, Talpaz M, Neamati N, Buckanovich RJ, Leukemia inhibitory factor functions in parallel with interleukin-6 to promote ovarian cancer growth. Oncogene 38, 1576–1584 (2019). [PubMed: 30305729]
30. Iwamaru A, Szymanski S, Iwado E, Aoki H, Yokoyama T, Fokt I, Hess K, Conrad C, Madden T, Sawaya R, Kondo S, Priebe W, Kondo Y, A novel inhibitor of the STAT3 pathway induces apoptosis in malignant glioma cells both in vitro and in vivo. Oncogene 26, 2435–2444 (2007). [PubMed: 17043651]

31. Hussain SF, Kong LY, Jordan J, Conrad C, Madden T, Fokt I, Priebe W, Heimberger AB, A novel small molecule inhibitor of signal transducers and activators of transcription 3 reverses immune tolerance in malignant glioma patients. Cancer Res 67, 9630–9636 (2007). [PubMed: 17942891]
32. Daina A, Michielin O, Zoete V, SwissADME: a free web tool to evaluate pharmacokinetics, drug-likeness and medicinal chemistry friendliness of small molecules. Sci Rep 7, 42717 (2017).
33. Kong LY, Abou-Ghazal MK, Wei J, Chakraborty A, Sun W, Qiao W, Fuller GN, Fokt I, Grimm EA, Schmittling RJ, Archer GE Jr., Sampson JH, Priebe W, Heimberger AB, A novel inhibitor of signal transducers and activators of transcription 3 activation is efficacious against established central nervous system melanoma and inhibits regulatory T cells. Clin Cancer Res 14, 5759–5768 (2008). [PubMed: 18794085]
34. Gao L, Li FS, Chen XH, Liu QW, Feng JB, Liu QJ, Su X, Radiation induces phosphorylation of STAT3 in a dose- and time-dependent manner. Asian Pac J Cancer Prev 15, 6161–6164 (2014). [PubMed: 25124591]
35. Spitzner M, Ebner R, Wolff HA, Ghadimi BM, Wienands J, Grade M, STAT3: A Novel Molecular Mediator of Resistance to Chemoradiotherapy. Cancers (Basel) 6, 1986–2011 (2014). [PubMed: 25268165]
36. Xie B, Zhang L, Hu W, Fan M, Jiang N, Duan Y, Jing D, Xiao W, Fragoso RC, Lam KS, Sun LQ, Li JJ, Dual blockage of STAT3 and ERK1/2 eliminates radioresistant GBM cells. Redox Biol 24, 101189 (2019).
37. Chen CCL, Deshmukh S, Jessa S, Hadjadj D, Lisi V, Andrade AF, Faury D, Jawhar W, Dali R, Suzuki H, Pathania M, Dubois DA,F, Woodward E, Hebert S, Coutelier M, Karamchandani J, Albrecht S, Brandner S, De Jay N, Gayden T, Bajic A, Harutyunyan AS, Marchione DM, Mikael LG, Juretic N, Zeinieh M, Russo C, Maestro N, Bassenden AV, Hauser P, Virga J, Bognar L, Klekner A, Zapotocky M, Vicha A, Krskova L, Vanova K, Zamecnik J, Sumerauer D, Ekert PG, Ziegler DS, Ellezam B, Filbin MG, Blanchette M, Hansford JR, Khuong-Quang DA, Berghuis AM, Weil AG, Garcia BA, Garzia L, Mack SC, Beroukhim R, Ligon KL, Taylor MD, Bandopadhayay P, Kramm C, Pfister SM, Korshunov A, Sturm D, Jones DTW, Salomoni P, Kleinman CL, Jabado N, Histone H3.3G34-Mutant Interneuron Progenitors Co-opt PDGFRA for Gliomagenesis. Cell 183, 1617–1633 e1622 (2020). [PubMed: 33259802]
38. Funato K, Smith RC, Saito Y, Tabar V, Dissecting the impact of regional identity and the oncogenic role of human-specific NOTCH2NL in an hESC model of H3.3G34R-mutant glioma. Cell Stem Cell 28, 894–905 e897 (2021). [PubMed: 33631117]
39. Bressan RB, Southgate B, Ferguson KM, Blin C, Grant V, Alfazema N, Wills JC, Marques-Torrejon MA, Morrison GM, Ashmore J, Robertson F, Williams CAC, Bradley L, von Kriegsheim A, Anderson RA, Tomlinson SR, Pollard SM, Regional identity of human neural stem cells determines oncogenic responses to histone H3.3 mutants. Cell Stem Cell 28, 877–893 e879 (2021). [PubMed: 33631116]
40. Dhayalan A, Rajavelu A, Rathert P, Tamas R, Jurkowska RZ, Ragozin S, Jeltsch A, The Dnmt3a PWWP domain reads histone 3 lysine 36 trimethylation and guides DNA methylation. J Biol Chem 285, 26114–26120 (2010). [PubMed: 20547484]
41. Sharifi-Zarchi A, Gerovska D, Adachi K, Totonchi M, Pezeshk H, Taft RJ, Scholer HR, Chitsaz H, Sadeghi M, Baharvand H, Arauzo-Bravo MJ, DNA methylation regulates discrimination of enhancers from promoters through a H3K4me1-H3K4me3 seesaw mechanism. BMC Genomics 18, 964 (2017). [PubMed: 29233090]
42. Huynh J, Chand A, Gough D, Ernst M, Therapeutically exploiting STAT3 activity in cancer - using tissue repair as a road map. Nat Rev Cancer 19, 82–96 (2019). [PubMed: 30578415]
43. Vignais ML, Sadowski HB, Watling D, Rogers NC, Gilman M, Platelet-derived growth factor induces phosphorylation of multiple JAK family kinases and STAT proteins. Mol Cell Biol 16, 1759–1769 (1996). [PubMed: 8657151]
44. Harhous Z, Booz GW, Ovize M, Bidaux G, Kurdi M, An Update on the Multifaceted Roles of STAT3 in the Heart. Front Cardiovasc Med 6, 150 (2019). [PubMed: 31709266]
45. Masliantsev K, Pinel B, Balbous A, Guichet PO, Tachon G, Milin S, Godet J, Duchesne M, Berger A, Petropoulos C, Wager M, Karayan-Tapon L, Impact of STAT3 phosphorylation in glioblastoma stem cells radiosensitization and patient outcome. Oncotarget 9, 3968–3979 (2018). [PubMed: 29423098]

46. Verstovsek S, Manshouri T, Quintas-Cardama A, Harris D, Cortes J, Giles FJ, Kantarjian H, Priebe W, Estrov Z, WP1066, a novel JAK2 inhibitor, suppresses proliferation and induces apoptosis in erythroid human cells carrying the JAK2 V617F mutation. Clin Cancer Res 14, 788–796 (2008). [PubMed: 18245540]

47. Grasso CS, Tang Y, Truffaux N, Berlow NE, Liu L, Debily MA, Quist MJ, Davis LE, Huang EC, Woo PJ, Ponnuswami A, Chen S, Johung TB, Sun W, Kogiso M, Du Y, Qi L, Huang Y, Hutt-Cabezas M, Warren KE, Le Dret L, Meltzer PS, Mao H, Quezado M, van Vuurden DG, Abraham J, Fouladi M, Svalina MN, Wang N, Hawkins C, Nazarian J, Alonso MM, Raabe EH, Hulleman E, Spellman PT, Li XN, Keller C, Pal R, Grill J, Monje M, Functionally defined therapeutic targets in diffuse intrinsic pontine glioma. Nat. Med, (2015).

48. Bayliss J, Mukherjee P, Lu C, Jain SU, Chung C, Martinez D, Sabari B, Margol AS, Panwalkar P, Parolia A, Pekmezci M, McEachin RC, Cieslik M, Tamrazi B, Garcia BA, La Rocca G, Santi M, Lewis PW, Hawkins C, Melnick A, David Allis C, Thompson CB, Chinnaiyan AM, Judkins AR, Venneti S, Lowered H3K27me3 and DNA hypomethylation define poorly prognostic pediatric posterior fossa ependymomas. Sci Transl Med 8, 366ra161 (2016).

49. Li S, Garrett-Bakelman FE, Akalin A, Zumbo P, Levine R, To BL, Lewis ID, Brown AL, D'Andrea RJ, Melnick A, Mason CE, An optimized algorithm for detecting and annotating regional differential methylation. BMC Bioinformatics 14 Suppl 5, S10 (2013).

50. Yu G, Wang LG, He QY, ChIPseeker: an R/Bioconductor package for ChIP peak annotation, comparison and visualization. Bioinformatics 31, 2382–2383 (2015). [PubMed: 25765347]

51. Mi H, Muruganujan A, Ebert D, Huang X, Thomas PD, PANTHER version 14: more genomes, a new PANTHER GO-slim and improvements in enrichment analysis tools. Nucleic Acids Res 47, D419–D426 (2019). [PubMed: 30407594]

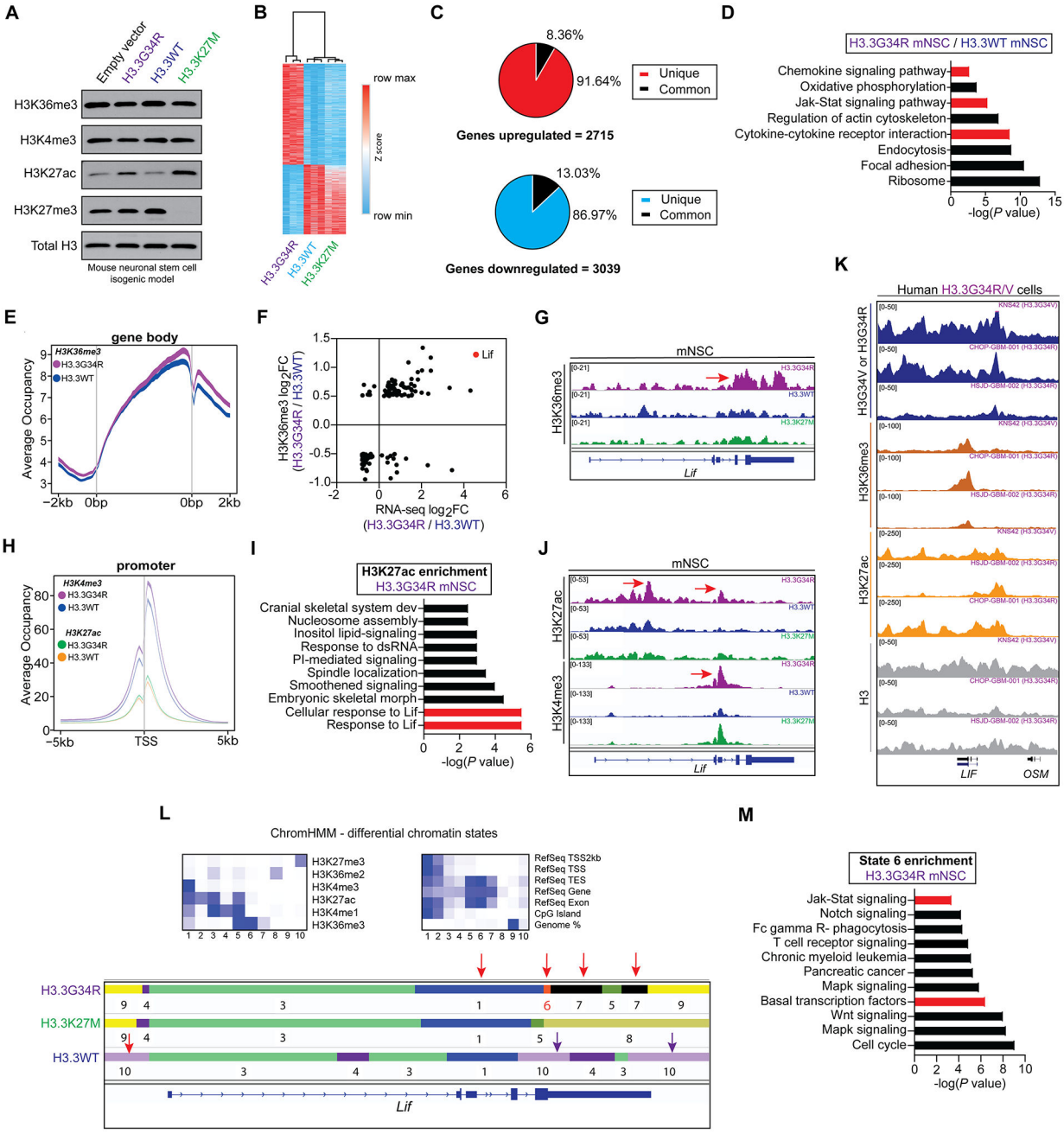

Figure 1. H3.3G34R/V cells exhibit transcriptomic and epigenetic alterations converging on the LIF/JAK/STAT3 axis.

(**A**) Western blots of parental mNSCs stably transduced with HA-tagged H3.3G34R, H3.3WT, and H3.3K27M expression plasmids for H3K36me3, H3K4me3, H3K27ac, H3K27me3, and total H3. (**B**) Heatmap of differentially expressed genes determined by RNA-seq in H3.3G34R, H3.3WT, and H3.3K27M mNSCs. (**C**) RNA-seq analysis comparing H3.3G34R/H3.3WT and H3.3K27M/H3.3WT mNSCs demonstrating upregulated/downregulated genes unique to H3.3G34R and shared with H3.3K27M mNSCs. (**D**) Gene set enrichment analysis (GSEA) for genes upregulated in H3.3G34R mNSCs

compared to H3.3WT mNSCs. (**E**) Average H3K36me3 occupancy (Y-axis) at gene bodies in H3.3G34R and H3.3WT mNSCs. (**F**) H3K36me3 enrichment in H3.3G34R/H3.3WT mNSCs (log_2 fold-change, Y-axis plotted against H3.3G34R/H3.3WT gene expression (log_2 fold-change, X-axis) for genes with differential H3K36me3. (**G**) Integrated Genomics Viewer (IGV) snapshot of H3K36me3 enrichment at the *Lif* gene body in H3.3G34R (purple), H3.3WT (blue), and H3.3K27M (green) mNSCs. Red arrow demonstrates enrichment in H3.3G34R mNSCs. (**H**) Average H3K27ac and H3K4me3 occupancy (Y-axis) at gene promoters (defined as +/− 5kb from TSS, X-axis) in H3.3G34R and H3.3WT mNSCs. (**I**) Pathway analysis for genes with differential deposition of H3K27ac in H3.3G34R mNSCs versus H3.3WT mNSCs. *P* values are indicated from PANTHER-GO analysis of promoter H3K27ac-enriched genes. (**J**) IGV snapshot of H3K27ac and H3K4me3 enrichment at the *Lif* promoter in H3.3G34R (purple), H3.3WT (blue), and H3.3K27M (green) mNSCs. Red arrow demonstrates enrichment in H3.3G34R mNSCs. (**K**) IGV snapshot of H3.3G34R or H3.3G34V (blue), H3K36me3 (brown), H3K27ac (orange), and total H3 (gray) enrichment at *LIF* in H3.3G34V (KNS42) and H3.3G34R (CHOP-GBM-001 and HSJD-GBM-002) cells. (**L**) ChromHMM heatmaps illustrating combinatorial patterns of histone epigenetic modifications, H3K36me3, H3K4me1, H3K27ac, H3K4me3, H3K36me2, and H3K27me3, used to assign 10 distinct chromatin states (*top left*). Chromatin states are related to each genomic region (CpG islands, exons, transcription start sites) such that each region is associated with its most representative state (*top right*). Defined chromHMM states assigned to regions of the *Lif* locus (*bottom*) in H3.3G34R, H3.3WT, and H3.3K27M mNSCs. Note that State 6 (orange) is present only in H3.3G34R cells, State 10 (light purple) is present exclusively in H3.3WT mNSCs, and State 1 (blue) is more widely represented in H3.3G34R mNSCs versus both H3.3WT and H3.3K27M mNSCs. Red arrows indicate enrichment of H3K36me3-containing chromHMM states in H3.3G34R mNSCs. Purple arrows indicate regions with repressive H3K27me3-containing chromHMM state 10 in H3.3WT mNSCs. (**M**) Pathway analysis for genes demonstrating chromHMM state 6 enrichment in H3.3G34R mNSCs when compared to the same genomic regions in H3.3WT mNSCs. *P* values are indicated from gene set enrichment analysis (GSEA) of genes with specific State 6 enrichment in H3.3G34R mNSCs.

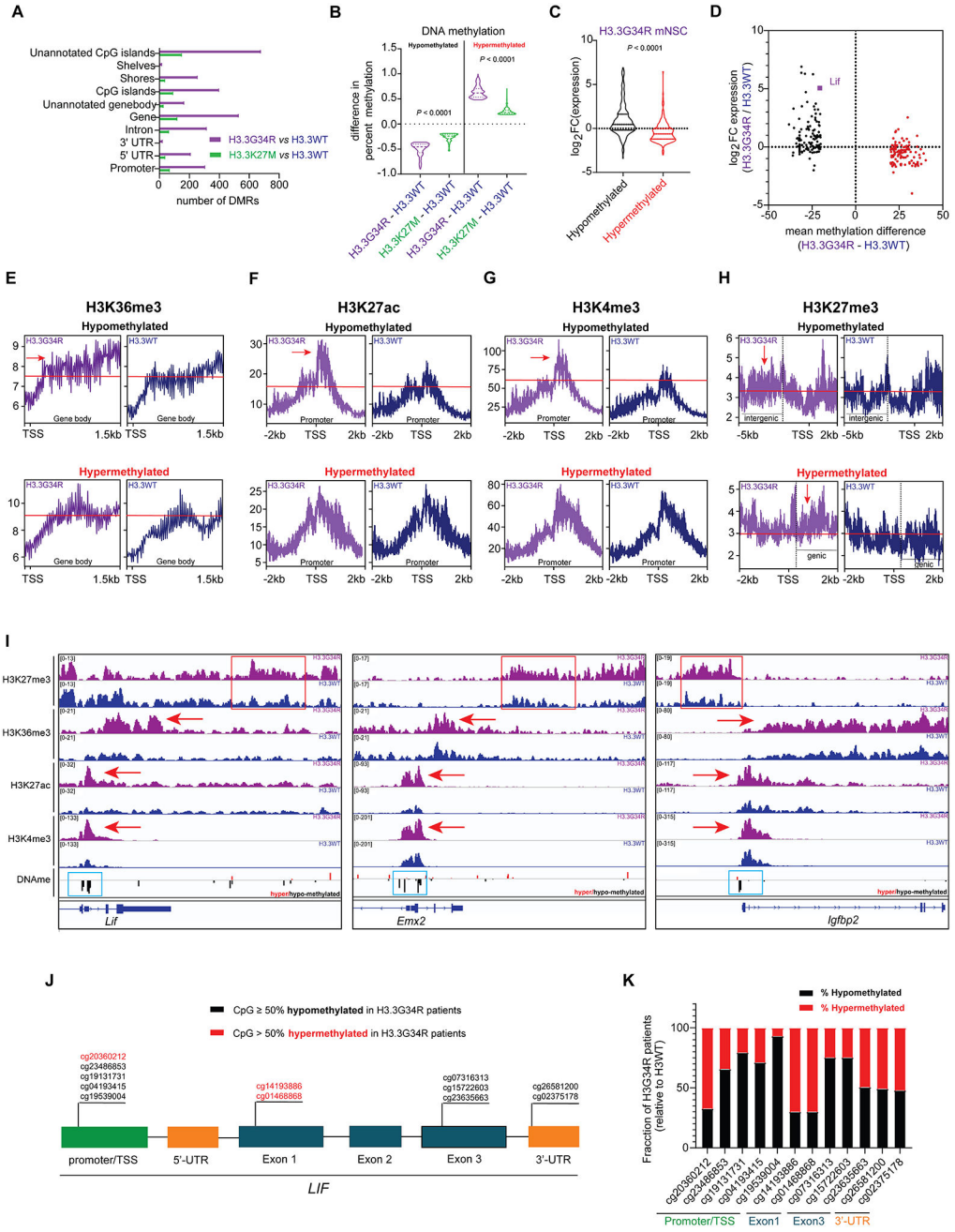

Figure 2. H3.3G34R/V alters DNA methylation and H3K27me3 at the *LIF* locus.

(**A**) Comparison of differentially methylated genomic regions (DMRs) in H3.3G34R versus H3.3WT mNSCs. (**B**) Violin plots depicting the difference in percent methylation for the 500 most hypomethylated or hypermethylated CpG sites within promoters in H3.3G34R (purple) versus H3.3WT and H3.3K27M (green) versus H3.3WT mNSCs. (**C**) Violin plot depicting associated $\log_2$ fold-change in mRNA expression of the 500 most hypomethylated and hypermethylated promoter CpG sites in H3.3G34R mNSCs. (**D**) X-Y plot for $\log_2$ fold-change in mRNA expression (Y-axis) and mean methylation difference (X-axis) in H3.3G34R versus H3.3WT mNSCs. (**E-H**) Average H3K36me3 occupancy at gene bodies

(**E**); H3K27ac (**F**) and H3K4me3 (**G**) enrichment at promoter regions; and H3K27me3 (**H**) occupancy at promoter and flanking region in H3.3G34R mNSCs for gene loci with promoter hypomethylation (*top*) or hypermethylation (*bottom*) in H3.3G34R (purple) versus H3.3WT (blue) mNSCs. Red arrows indicate enrichment of the histone modification. Black bars denote intergenic and genic regions. (**I**) Integrated Genomics Viewer snapshot of H3K27me3, H3K36me3, H3K27ac, and H3K4me3 ChIPseq signals plotted with DNA methylation (relative to H3.3WT mNSCs; black, hypomethylated; red, hypermethylated) at *Lif, Emx2*, and *Igfbp2* in H3.3G34R (purple) and H3.3WT (blue) mNSCs. Red boxes indicate gain of H3K27me3 in intergenic regions. Red arrows indicate gain of activating epigenetic marks at gene promoters and gene bodies. Blue boxes indicate DNA hypomethylation at the gene promoter. (**J**) Schematic of human *LIF* structure indicating CpG site genomic locations. Sites indicated in black and red indicate greater than 50 percent of H3.3G3R patients with hypomethylated or hypermethylation, respectively, of the CpG site relative to H3.3WT glioma patients. (**K**) Bar graphs showing the proportion of H3.3G34R glioma patients (n=73) with hypomethylation (black) or hypermethylation (red) of CpG sites within *LIF* relative to H3.3WT (n=1306) glioma patients. Data in (**B**) and (**C**) analyzed by parametric, 2-sided, unpaired, Student's *t* test.

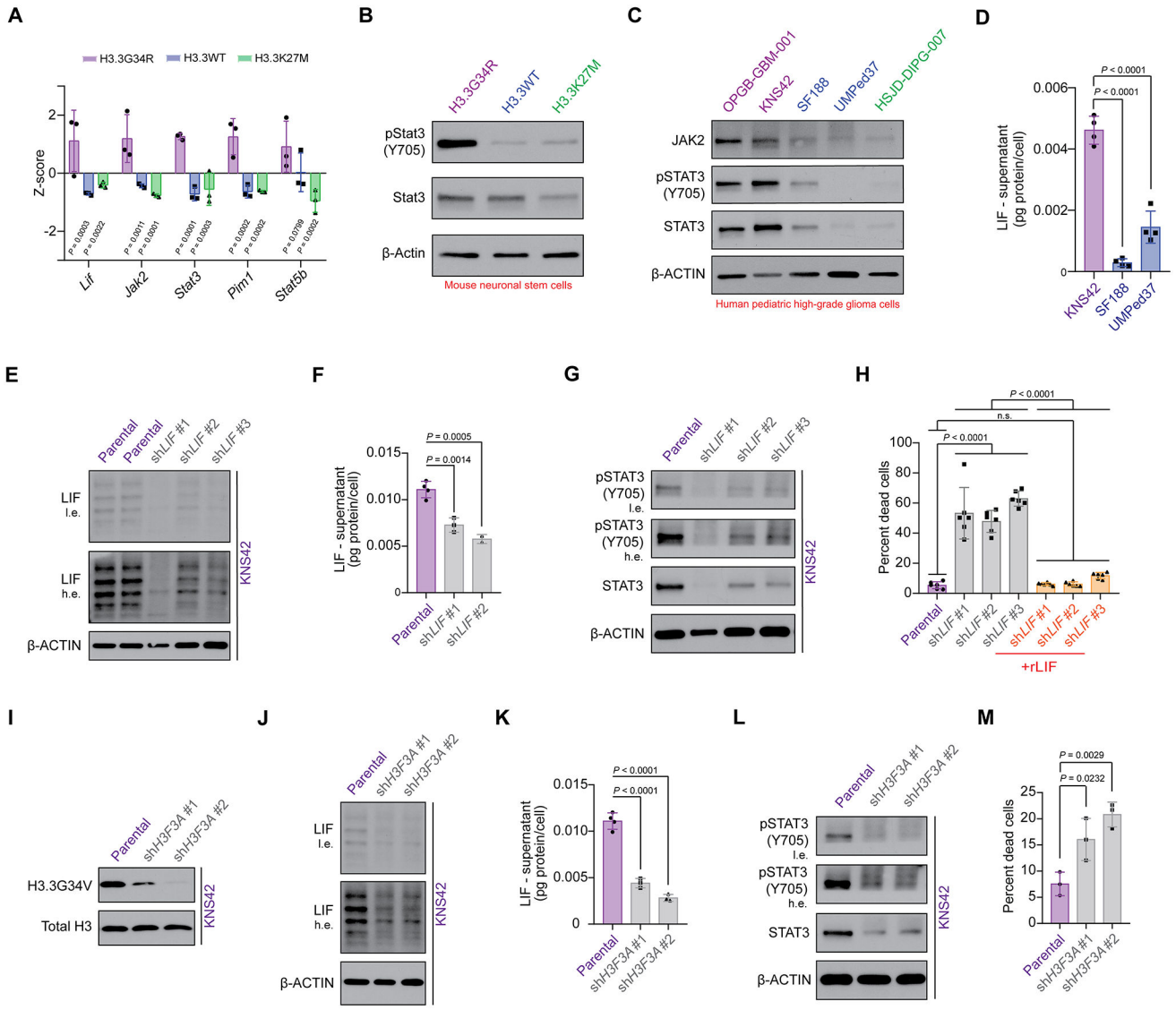

Figure 3. H3.3G34R/V mutations drive STAT3 signaling via elevated LIF secretion.

(**A**) Bar plot of differentially expressed genes (Z-score, Y-axis) *Lif, Jak2, Stat3, Pim1*, and *Stat5b* assessed by RNA sequencing in H3.3G34R (purple), H3.3WT (blue), and H3.3K27M (green) mNSCs; n=3 biological replicates. (**B**) Representative Western blots of cell lysates from mNSCs stably transduced with H3.3G34R, H3.3WT, and H3.3K27M transgenes for pStat3(Y705), Stat3, and β-Actin. (**C**) Representative Western blots on cell lysates from pHGG cell lines OPGB-GBM-001 (H3.3G34R), KNS42 (H3.3G34V), SF188 (H3.3WT), UMPed37 (H3.3WT), and HSJD-DIPG-007 (H3.3K27M) for JAK2, pSTAT3(Y705), STAT3, and β-ACTIN. (**D**) ELISA for human LIF protein (pg protein/cell, Y-axis) in cell supernatants in H3.3G34V KNS42 cells compared to H3.3WT SF188 and UMPed37 cells after 4 days in culture; n=4 technical replicates. (**E**) Representative Western blots for LIF and β-ACTIN in KNS42 stably transduced with non-targeted (NT) or three independent *LIF* shRNAs; l.e. = low exposure, h.e. = high exposure. (**F**) ELISA of human LIF protein (pg protein/cell, Y-axis) in cell supernatants in KNS42 cells from (**E**) with or

without LIF knockdown; *n*=3–4 technical replicates. (**G**) Representative Western blots of KNS42 cells stably transduced with three independent *LIF* shRNAs for pSTAT3(Y705), STAT3, and β-ACTIN; l.e. = low exposure, h.e. = high exposure. (**H**) Percent dead cells (Y-axis) in KNS42 parental cells (purple bar), LIF-knockdown cells from (**G**) (gray bars), or knockdown cells in the presence of recombinant human LIF (rLIF, 50 ng/mL, orange bars); *n*=6 technical replicates. (**I**) Representative Western blots for mutant specific-H3.3G34V and total H3 in KNS42 stably transduced with two independent *H3F3A* shRNAs. (**J**) Representative Western blots for LIF and β-ACTIN in cells from (**I**); l.e. = low exposure, h.e. = high exposure. (**K**) ELISA for human LIF protein (pg protein/cell, Y axis) in KNS42 cells from (**I**) with or without *H3F3A* knockdown; *n*=3–4 technical replicates. (**L**) Representative Western blots of KNS42 cells stably transduced with two independent *H3F3A* shRNAs for pSTAT3(Y705), STAT3, and β-ACTIN; l.e. = low exposure, h.e. = high exposure. (**M**) Percent dead cells (Y-axis) in KNS42 cells with or without *H3F3A* knockdown from (**L**); *n*=3 technical replicates. Data in (**A**), (**D**), (**F**), (**H**), (**K**), and (**M**) are plotted as mean +/− S.D. Data in (**A**) are analyzed by two-way ANOVA with Dunnett's multiple comparisons test. Data in (**D**), (**F**), (**H**), (**K**), and (**M**) are analyzed by one-way ANOVA with Dunnett's multiple comparisons test.

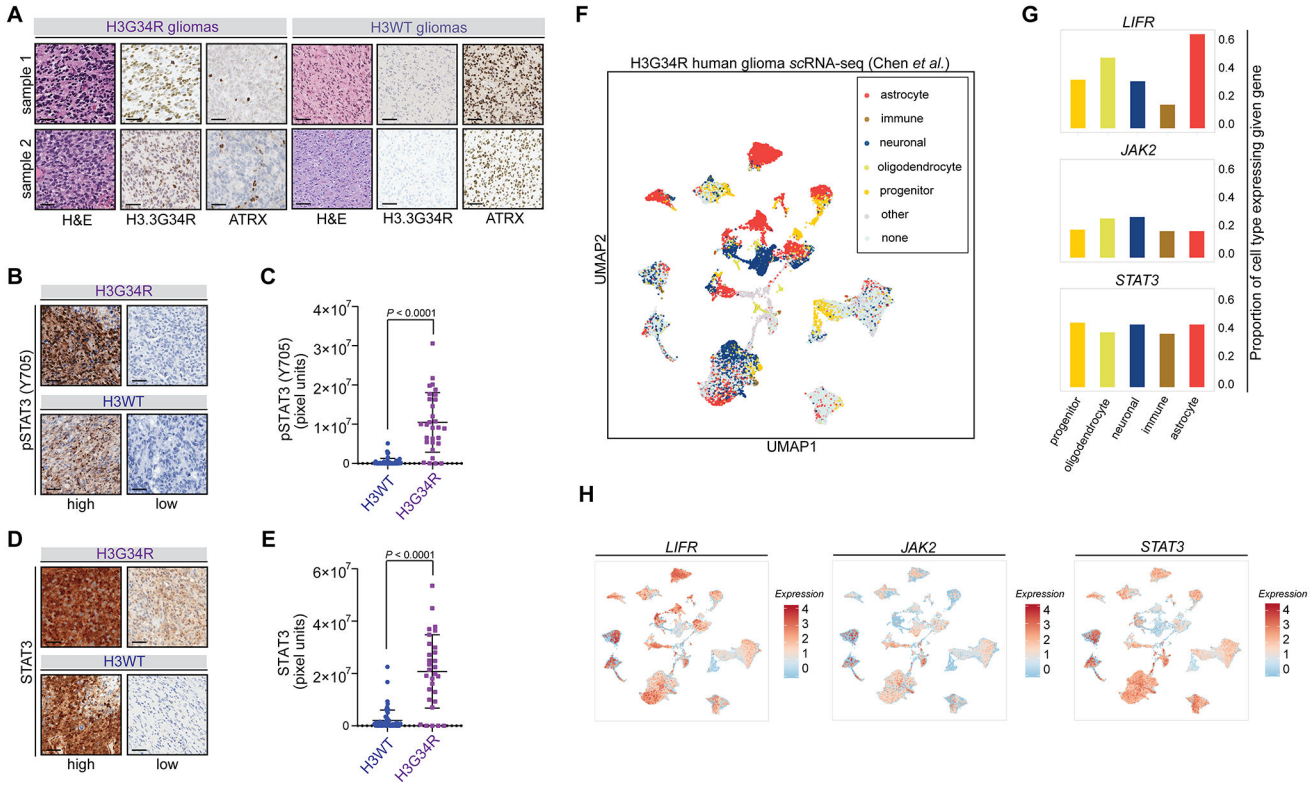

Figure 4. H3.3G34R/V patient-derived tumor cells and tissues exhibit robust STAT3 expression and pathway activation.

(**A**) Representative IHC images of two H3.3G34R (purple, *left*) and two H3WT (blue, *right*) human high-grade glioma tumors stained with Hematoxylin and eosin (H&E), mutant-specific H3.3G34R, or ATRX. Scale bar, 60 μm. (**B**) Representative IHC images from human H3.3G34R (*top*) or H3WT (*bottom*) gliomas for pSTAT3(Y705). IHC images demonstrating the highest and lowest pSTAT3(Y705) staining within each cohort were selected. Scale bar, 60 μm. (**C**) Blinded quantification (pixel units, Y-axis) of pSTAT3(Y705) staining in H3WT (blue) and H3.3G34R (purple) human glioma samples. H3.3G34R, n=6 samples; H3WT, n=12 samples. Five randomly selected regions were imaged per sample. Each dot represents the quantification of a single image from each tumor within each cohort. (**D**) Representative IHC images from human H3.3G34R (*top*) or H3WT (*bottom*) gliomas for total STAT3. IHC images demonstrating the highest and lowest STAT3 staining within each cohort were selected. Scale bar, 60 μm. (**E**) Blinded quantification (pixel units, Y-axis) of STAT3 staining in H3WT (blue) and H3.3G34R (purple) human glioma samples. H3.3G34R, n=6 samples; H3WT, n=12 samples. Five randomly selected regions were imaged per sample. Each dot represents the quantification of a single image from each tumor within each cohort. (**F**) Uniform manifold approximation and projection (UMAP) embedding of scRNA-seq data from malignant H3.3G34R/V cells originating from sixteen patient samples (14 patients, two primary-recurrence pairs) analyzed in Chen *et al.* (2020). Cells are colored by most similar normal brain cell type.

(**G**) Bar plots illustrating the proportion of each cell type aggregated from all tumors (progenitor, yellow; oligodendrocyte, green; neuronal, blue; immune, brown; astrocyte, red)

expressing the given JAK/STAT pathway genes *LIFR* (*top*), *JAK2* (*center*), and *STAT3* (*bottom*). (**H**) UMAP embedding of scRNA-seq data of malignant H3.3G34R/V cells as in (**F**), with cells colored by expression of *LIFR*, *JAK2*, or *STAT3*. Data in (**C**) and (**E**) are plotted as mean +/− S.D. and analyzed by parametric, 2-sided, unpaired, Student's *t* test.

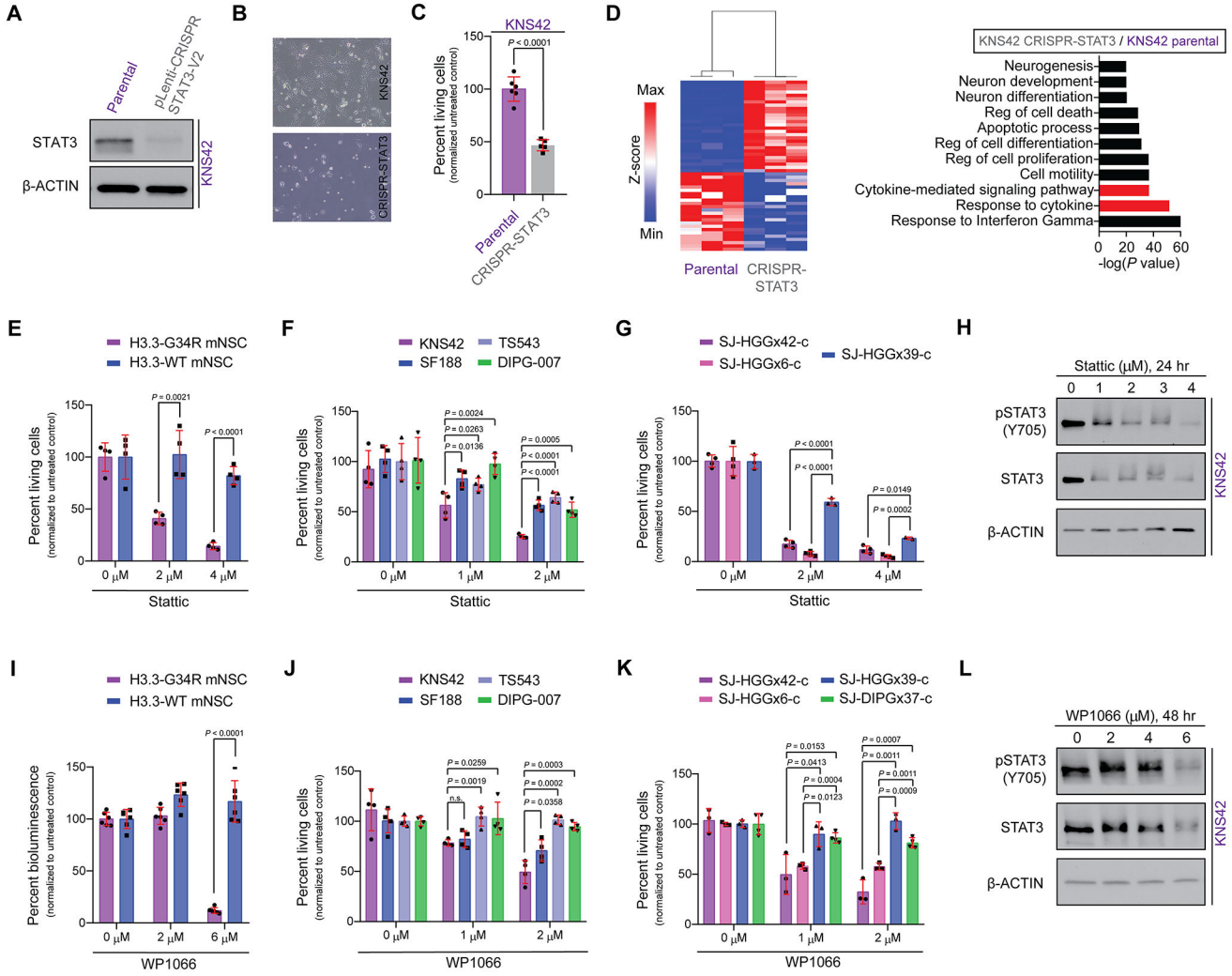

Figure 5. STAT3 inhibition demonstrates greater toxicity in H3.3G34R/V compared to H3.3WT glioma cells in vitro.

(**A-B**) Representative Western blots (**A**) and bright field images (**B**) of H3.3G34V KNS42 cells with or without CRISPR-mediated *STAT3* knockout. (**C**) Cell counts (percentage of living cells, Y-axis; cell line condition, X-axis) in H3.3G34V KNS42 cells with or without *STAT3* knockout from (**B**) after 6 days in culture; n=6 technical replicates. (**D**) Heatmap and GSEA of differentially expressed genes determined by RNA-seq in H3.3G34V KNS42 cells with or without *STAT3* knockout; n=3 technical replicates. (**E-F**) Cell counts (percentage of living cells, Y-axis; drug concentrations, X-axis) of H3.3G34R (purple) and H3.3WT (blue) mNSCs (**E**); and H3.3G34V KNS42 (purple), H3.3WT SF188 (blue), H3.3WT TS543 (lavender) and H3.3K27M HSJD-DIPG-007 (green) patient-derived pHGG cells (**F**) treated with STAT3 inhibitor, Stattic, for 96 hours at indicated concentrations. n=4 technical replicates. (**G**) Cell counts (percentage of living cells, Y-axis; drug concentrations, X-axis) of H3.3G34R SJ-HGGx42-c (purple), H3.3G34R SJ-HGGx6-c (pink), and H3.3WT SJ-HGGx39-c patient-derived pHGG cells treated with Stattic for 96 hours at indicated concentrations. n=3 technical replicates. (**H**) Representative Western blots for pSTAT3(Y705), STAT3, and β-ACTIN in H3.3G34V KNS42 cells

treated with Stattic for 24 hours at indicated concentrations. (**I**) Cell counts (percentage of bioluminescence signal, Y-axis; drug concentrations, X-axis) of H3.3G34R (purple) and H3.3WT (blue) mNSCs treated with STAT3 inhibitor, WP1066, for 96 hours at indicated concentrations. *n*=4 technical replicates. (**J**) Cell counts (percentage of living cells, Y-axis; drug concentrations, X-axis) of H3.3G34V KNS42 (purple), H3.3WT SF188 (blue), H3.3WT TS543 (lavender) and H3.3K27M HSJD-DIPG-007 (green) patient-derived pHGG cells treated with STAT3 inhibitor, WP1066, for 96 hours at indicated concentrations. *n*=4 technical replicates. (**K**) Cell counts (percentage of living cells, Y-axis; drug concentrations, X-axis) of H3.3G34R SJ-HGGx42-c (purple), H3.3G34R SJ-HGGx6-c (pink), H3.3WT SJ-HGGx39-c (blue), and H3.3K27M SJ-DIPGx37-c (green) human patient-derived pHGG cells treated with WP1066 for 96 hours at indicated concentrations; *n*=3–4 technical replicates. (**L**) Representative Western blot for pSTAT3(Y705), STAT3, and β-ACTIN in KNS42 cells treated with WP1066 for 48 hours at indicated concentrations. Responses of each cell line in (**C**), (**E**), (**F**), (**G**), (**I**), (**J**), and (**K**) are plotted as percent of living cells relative to corresponding untreated control. Data in (**C**), (**E**), (**F**), (**G**), (**I**), (**J**), and (**K**) are plotted as mean +/− S.D. and analyzed by parametric, 2-sided, unpaired, Student's *t* test.

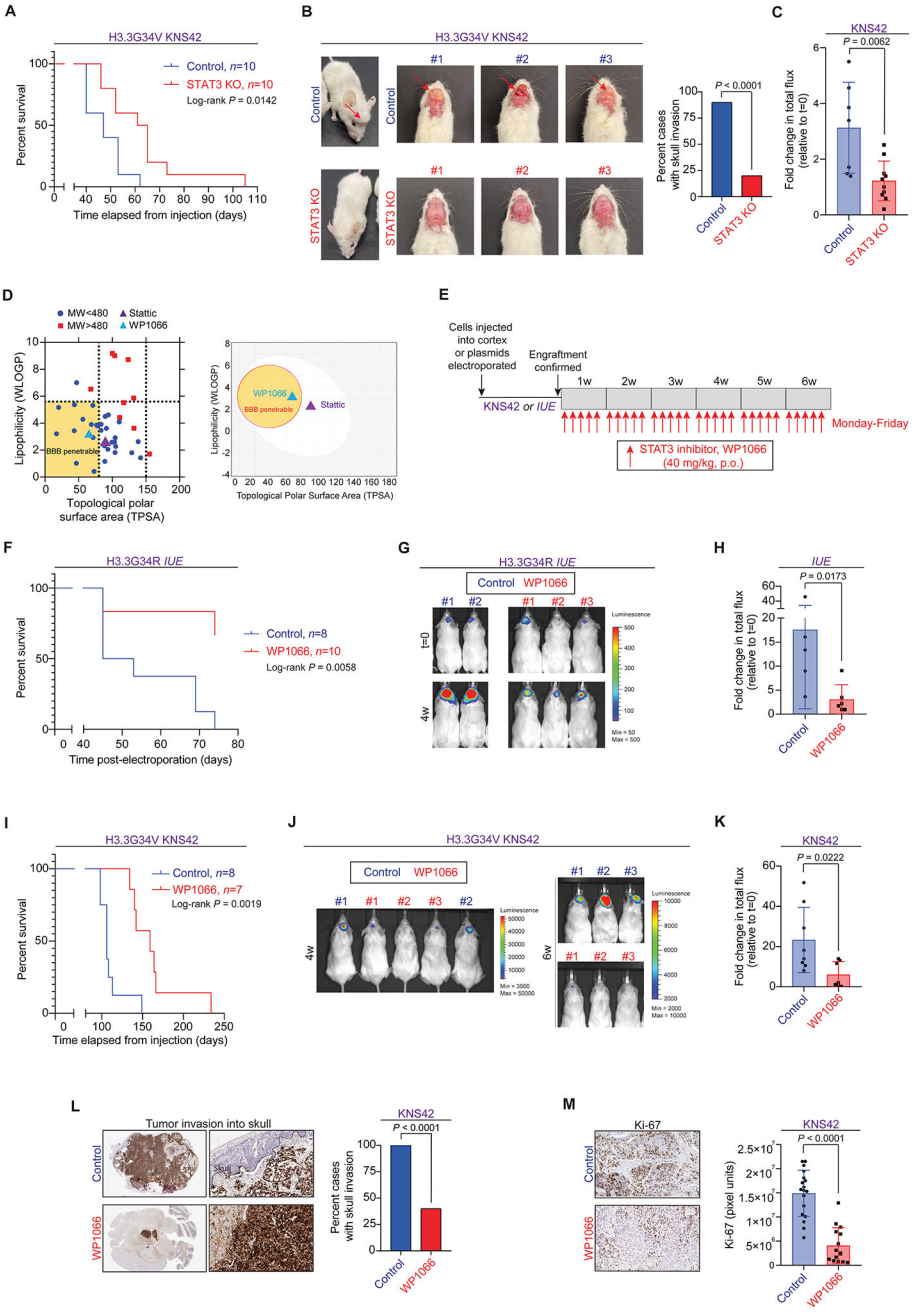

Figure 6. Inhibition of STAT3 activity is therapeutic in H3.3G34R/V glioma models in vivo.

(**A**) Kaplan-Meier analysis of mice harboring H3.3G34V KNS42 tumors with and without *STAT3* genetic knockout (*STAT3* KO) as a function of time post-implantation. Control, blue, *n*=10; *STAT3* KO animals, red, *n*=10. (**B**) Representative images of tumor invasion into the skull (red arrows) in mice bearing KNS42 tumors with or without *STAT3* KO (*left*). Bar graph illustrates percent of mice within control and *STAT3* KO cohorts with observable tumor invasion into the skull (*right*). Control, blue, *n*=5; STAT3 KO, red, *n*=10. (**C**) Bioluminescent signal quantification (Y-axis) of animals from (**A**) at week 5 post-implantation. Fold change in total flux was calculated by normalizing bioluminescent

signal at the given time point by the corresponding baseline signal for each mouse. Each symbol represents one mouse. Control, blue, *n*=7; *STAT3* KO animals, red, *n*=10. (**D**) X-Y plot illustrating relative molecular weight (MW < 480 g/mol, dark blue; MW > 480 g/mol, red), lipophilicity (WLOGP value, Y-axis), and topological polar surface area (TPSA, X-axis) characteristics of available STAT3 inhibitors (*left*). The SwissADME model developed by the Swiss Institute of Bioinformatics was utilized to generate the pharmacokinetic and ADME properties illustrated on the plot (32). Shaded yellow area represents chemical properties associated with predicted BBB penetrability; WP1066 (light blue triangle) and Stattic (purple triangle) are indicated. A BOILED-Egg X-Y plot demonstrating the lipophilicity (WLOGP, Y-axis) and topological polar surface area (TPSA, X-axis) of STAT3 inhibitors Stattic (purple triangle) and WP1066 (blue triangle) (*right*). Yellow area defines the range of WLOGP and TPSA properties for inhibitors with predicted BBB penetrability and white area defines the range of WLOGP and TPSA properties associated with predicted gastrointestinal absorption. (**E**) WP1066 treatment paradigm for animals (1) orthotopically implanted with H3.3G34V KNS42 cells or (2) animals bearing H3.3G34R tumors established via *in-utero* electroporation (*IUE*). H3.3G34R *IUE* tumors were established in CD-1 mice with expression plasmids for dominant-negative *Tp53*, mutant *Pdgfra-D842V*, and mutant H3.3G34R *H3f3a*. Red arrows indicate WP1066 administration via oral gavage over a six-week period. (**F**) Kaplan-Meier analysis of H3.3G34R *IUE* tumor-bearing mice treated with WP1066 as a function of time post-electroporation. Control, blue, *n*=8; WP1066-treated animals, red, *n*=10. (**G**) Representative bioluminescent images from H3.3G34R *IUE* control and WP1066-treated mice before (t=0) and after four (4w) weeks WP1066 treatment. (**H**) Bioluminescent signal quantification of H3.3G34R *IUE* tumor-bearing mice receiving WP1066 or vehicle in (**F**). Fold change in total flux (Y-axis) is calculated by normalizing bioluminescent signal at treatment time point by corresponding baseline signal before treatment for each mouse. Each symbol represents one mouse. Control, blue, *n*=5; WP1066-treated animals, red, *n*=6. (**I**) Kaplan-Meier analysis of mice harboring H3.3G34V KNS42 tumors treated with WP1066 as a function of time post-implantation. Control, blue, *n*=8; WP1066-treated animals, red, *n*=7. (**J**) Representative bioluminescence images from animals implanted with H3.3G34V KNS42 cells in the cortex following four (4w) and six (6w) weeks of WP1066 treatment. (**K**) Bioluminescent signal quantification (Y-axis) of animals with H3.3G34V KNS42 tumors receiving WP1066 or vehicle in (**I**). Fold change in total flux is calculated by normalizing bioluminescent signal at treatment time point by the corresponding baseline signal before treatment for each mouse. Each symbol represents one mouse. Control, blue, *n*=8; WP1066-treated animals, red, *n*=7. (**L**) Representative IHC images of KNS42 cranial tumors stained for GFAP illustrating tumor invasion into the skull in mice (assessed in a blinded manner) with orthotopic H3.3G34V KNS42 tumors with or without WP1066 treatment (*left*). Bar graph illustrates percent of mice within control and treatment cohorts with observable tumor invasion into the skull *(right*). Note all control mice exhibit invasion. Control, blue, *n=8*; WP1066-treated animals, red, *n=7*.

(**M**) Representative IHC images and blinded quantification of Ki-67 (pixel units, Y-axis) in mice with orthotopic KNS42 tumors with or without WP1066 treatment (*left*). Bar plot represents quantification (pixel units, Y-axis) of three randomly selected regions per mouse, per treatment condition (*right*). Control, blue, *n*=6; WP1066-treated animals, red, *n*=5. Data

in (**C**), (**H**), (**K**), and (**M**) are plotted as mean +/− S.D., and data in (**B**), (**C**), (**H**), (**K**), (**L**), and (**M**) are analyzed by non-parametric, 2-sided, unpaired, Student's *t* test. Log-rank test was utilized in (**A**), (**F**), and (**I**) for Kaplan-Meier analysis (*P*-values are indicated for comparison with control animals).